

**Facile Synthesis of S-scheme  $\alpha$ -Fe<sub>2</sub>O<sub>3</sub>/BiOBr/MoS<sub>2</sub> Nano heterojunction with enhanced visible-light-induced photocatalytic activity for efficient Hydrogen production.**



By

**Rabia Nawaz**

(Registration No: 00000365116)

This thesis submitted to the National University of Sciences and Technology, Islamabad,

As a partial fulfillment of the requirements for the degree of

**Master of Science in Chemistry Thesis**

**Supervisor: Dr. Shahid Iqbal**

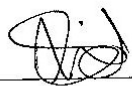
**Department of Chemistry, School of Natural Sciences**

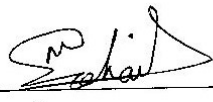
**National University of Sciences & Technology (NUST)**


**Islamabad, Pakistan**

**THESIS ACCEPTANCE CERTIFICATE**

Certified that final copy of MS thesis written by **Rabia Nawaz** (Registration No. **00000365116**), of **School of Natural Sciences** has been vetted by undersigned, found complete in all respects as per NUST statutes/regulations, is free of plagiarism, errors, and mistakes and is accepted as partial fulfillment for award of MS/M.Phil degree. It is further certified that necessary amendments as pointed out by GEC members and external examiner of the scholar have also been incorporated in the said thesis.

Signature:  \_\_\_\_\_  
Name of Supervisor: Dr. Shahid Iqbal \_\_\_\_\_  
Date: \_\_\_\_\_

Signature (HoD):  \_\_\_\_\_  
Date: 10/08/2023 \_\_\_\_\_

Signature (Dean/Principal):  \_\_\_\_\_  
Date: 11/10/23 \_\_\_\_\_

**National University of Sciences & Technology****MS THESIS WORK**

We hereby recommend that the dissertation prepared under our supervision by: Rabia Nawaz, Regn No. 00000365116 Titled: Facile Synthesis of  $\alpha$ - $\text{Fe}_2\text{O}_3/\text{BiOBr}/\text{MoS}_2$  Nanoheterojunction with Enhanced Visible Light Induced Photocatalytic Activity for Efficient  $\text{H}_2$  Production be Accepted in partial fulfillment of the requirements for the award of **MS** degree.

**Examination Committee Members**1. Name: DR. ASAD MUMTAZSignature: 2. Name: DR. MUHAMMAD ADIL MANSOORSignature: Supervisor's Name DR. SHAHID IQBALSignature:   
Head of Department10/08/2023  
Date**COUNTERSIGNED**Date: 11/8/23  
Dean/Principal

## **DEDICATION**

I affectionately dedicate this effort to all the members of my honorable family, especially to my parents, not forgetting my respected teachers and friends, who had a remarkable effort in this achievement.

**“Basic Research is what I am doing when I don’t know what I am doing”.**

WERNHER VON BRAUN

**Abstract**

A novel 2D-2D S-Scheme  $\alpha\text{-Fe}_2\text{O}_3$  / BiOBr /  $\text{MoS}_2$  heterojunction to act as photocatalyst for effective visible-light using photocatalytic applications is synthesized and characterized in this research. We used hydrothermal method to prepare our heterojunction ternary composite. The characterization used to check our composite were XRD, XPS, EDS, SEM, TEM, and HRTEM. Through DRS and PL, the material's optical characteristics were verified. The 2D-2D S-Scheme  $\alpha\text{-Fe}_2\text{O}_3/\text{BiOBr}/\text{MoS}_2$  ternary composite was applied for the development of photocatalytic hydrogen and the results showed excellent hydrogen production up to  $57 \text{ mmolh}^{-1} \text{ g}^{-1}$ . This ternary catalyst performed better than  $\alpha\text{-Fe}_2\text{O}_3$  and BiOBr by themselves.

## ACKNOWLEDGEMENTS

### BISMILLAHIRRAHMANIRRAHIM

Alhamdulillah, Praise be to Allah Almighty for the help and guidance that finally made me able to complete this thesis. First and foremost, I offer my sincerest gratitude to my supervisor **Dr. Shahid Iqbal**, Associate Professor, who has advised and guided me throughout my research with his patience and deepest knowledge.

- ❖ I would like to give my special thanks to my **friends** for sharing the ups and down throughout the completion of my research work and thesis. I pay my special regards and a lot of thanks to my **classmates** for their encouragement and support, especially at times when things were going tough.
- ❖ I cannot end without saying thanks to my family members, especially to my **parents** who supported me financially and encouraged me during my research work.

I hope, these studies will benefit to all of us.

## Contents

<b>Abstract</b> .....	<b>iii</b>
<b>List of figures</b> .....	<b>vii</b>
<b>Chapter 1: Introduction</b> .....	<b>1</b>
1.1 History .....	2
1.2 Challenges:.....	3
1.2.1 Energy Crisis.....	3
1.2.2 Present Fuel Options .....	3
1.3 Why Hydrogen?.....	6
1.4 Hydrogen as a Fuel .....	6
1.5 Photocatalysis .....	8
1.5.1 Types of Photocatalysis .....	9
Figure 4: Photocatalytic Reactions .....	12
Figure 5: Schematic diagram of hydrogen production through water splitting methodology over photocatalysts.....	13
1.6 Photocatalyst Selection for Hydrogen Production .....	16
1.7 Design to upgrade the photocatalyst efficiency .....	19
1.8 Heterojunction.....	21
1.9.1 Types of heterojunction .....	22
Figure 9: Type II heterojunction and Z-scheme photocatalysts' photocatalytic mechanisms	
Photocatalysts for type II heterojunction .....	24
1.9 S-scheme heterojunction .....	24
Figure 10: Charge Transfer Differences in Type-II and S-Scheme Heterojunctions.....	25
1.10 Modification.....	28
1.10.1 Modification of band locations of the semiconductor.....	29
1.11 Composing Nano-scale Catalyst .....	34
<b>Chapter 2: Literature Review</b> .....	<b>38</b>
<b>Chapter 3: Experimental</b> .....	<b>44</b>
3.1 Synthesis .....	44
3.2 Required precursors .....	44
3.3 Synthesis of $\alpha$ -Fe <sub>2</sub> O <sub>3</sub> nanosheets.....	45
3.4 Synthesis of BiOBr .....	46
3.5 Synthesis of MoS <sub>2</sub> .....	47
3.6 Establishment of $\alpha$ -Fe <sub>2</sub> O <sub>3</sub> / BiOBr .....	49
3.7 Establishment of $\alpha$ -Fe <sub>2</sub> O <sub>3</sub> /BiOBr/MoS <sub>2</sub> .....	49

<b>Chapter 4: Characterizations .....</b>	<b>51</b>
4.1 X-ray diffraction (XRD) .....	51
4.2 Scanning electron microscopy (SEM) .....	53
4.3 HR-TEM .....	55
4.4 Elemental Mapping .....	58
4.5 X-ray photoelectron spectroscopy (XPS) .....	59
4.6 Diffuse reflectance spectroscopy (DRS) .....	61
4.7 Photoluminescence Spectroscopy (PL Analysis) .....	63
4.8 Mott-Schotkey .....	65
4.9 Chronoamperometric Chopping .....	67
4.10 Mechanism Proposal .....	68
<b>Chapter 5: Hydrogen Production (Photocatalytic Activity) .....</b>	<b>71</b>
5.1 H <sub>2</sub> production by using Ethanol as a sacrificial agent .....	72
5.2 Comparison of Hydrogen production in Binary and Ternary Composites .....	73
5.3 Comparison of Hydrogen production in different morphologies of MoS <sub>2</sub> .....	74
5.4 Comparison with a different sacrificial agent .....	75
<b>Chapter 6: Conclusion .....</b>	<b>77</b>
<b>Future Prespective .....</b>	<b>79</b>
Hydrogen Storage .....	79
<b>Chapter 7: Refrences .....</b>	<b>80</b>



## List of figures

Figure 1: Hydrogen is utilized as a source of energy.....	5
Figure 2: Hydrogen production processes .....	8
Figure 3: Photocatalysis.....	10
Figure 4: Photocatalytic Reactions.....	13
Figure 5: Schematic illustration of hydrogen production through water splitting mechanism over photocatalysts.....	14
Figure 6: Band gap energy and band gap edge positions of different semiconductor oxides and oxyhalides, along with selected redox potentials.....	19
Figure 7: Schematic illustration of the electron-hole separation under the influence of the internal electric field of a p-n heterojunction photocatalyst under light irradiation.....	24
Figure 8: Schematic representation of different heterojunction photocatalysts.....	25
Figure 9: Photocatalytic mechanism of type II heterojunction and Z-scheme photocatalysts .....	26
Figure 10: Differentiation in Charge Transfer between Type-II and S-Scheme Heterojunctions.....	27
Figure 11: S-scheme heterojunction Photocatalyst.....	29
Figure 12: Synthesis of $\alpha$ -Fe <sub>2</sub> O <sub>3</sub> and BiOBr.....	51
Figure 13: Synthesis of MoS <sub>2</sub> .....	52
Figure 14: XRD pattern of $\alpha$ -Fe <sub>2</sub> O <sub>3</sub> , BiOBr, MoS <sub>2</sub> , $\alpha$ -Fe <sub>2</sub> O <sub>3</sub> / BiOBr and $\alpha$ -Fe <sub>2</sub> O <sub>3</sub> / BiOBr / MoS <sub>2</sub> .....	55
Figure 15: (a, b) ultrathin nanosheets of Fe <sub>2</sub> O <sub>3</sub> , (c, d) nanosheets of BiOBr, and (e, f) are SEM images of binary ( $\alpha$ -Fe <sub>2</sub> O <sub>3</sub> / BiOBr) composites.....	57
Figure 16: HR-TEM analysis of (a, b) few-layer nanosheets of MoS <sub>2</sub> , (c, d) Multi-layered nanosheets of MoS <sub>2</sub> , (e, f) MoS <sub>2</sub> nanoparticles.....	59
Figure 17: XPS spectrum of Fe 2p, C 1s, and O 1s.....	61
Figure 18: XPS spectrum of Bi 4f, Br 3d, Mo 3d, and S 2p.....	62
Figure 19: DRS Analysis of $\alpha$ -Fe <sub>2</sub> O <sub>3</sub> , BiOBr, MoS <sub>2</sub> , $\alpha$ -Fe <sub>2</sub> O <sub>3</sub> /BiOBr and $\alpha$ -Fe <sub>2</sub> O <sub>3</sub> /BiOBr/MoS <sub>2</sub> .....	64
Figure 20: Energy diagram showing absorption of light and the processes involved in the emission of light as fluorescence and phosphorescence.....	65
Figure 21: PL of Fe <sub>2</sub> O <sub>3</sub> , BiOBr and binary ( $\alpha$ -Fe <sub>2</sub> O <sub>3</sub> / BiOBr) composites.....	66
Figure 22: Mott-Schotkey Analysis of $\alpha$ -Fe <sub>2</sub> O <sub>3</sub> , BiOBr, MoS <sub>2</sub> , $\alpha$ -Fe <sub>2</sub> O <sub>3</sub> / BiOBr and $\alpha$ -Fe <sub>2</sub> O <sub>3</sub> / BiOBr / MoS <sub>2</sub> .....	69

Figure 23: Chronoamperometric Chopping of $\alpha$ -Fe <sub>2</sub> O <sub>3</sub> , BiOBr, MoS <sub>2</sub> , $\alpha$ -Fe <sub>2</sub> O <sub>3</sub> / BiOBr and $\alpha$ -Fe <sub>2</sub> O <sub>3</sub> / BiOBr / MoS <sub>2</sub> .....	70
Figure 24: S-scheme heterojunction between $\alpha$ -Fe <sub>2</sub> O <sub>3</sub> / BiOBr / MoS <sub>2</sub> .....	72
Figure 25: H <sub>2</sub> production by using Ethanol as a Sacrificial agent by different amounts of BiOBr loaded on Fe <sub>2</sub> O <sub>3</sub> .....	74
Figure 26: Comparison of Hydrogen Production in Binary and Ternary Composites.....	75
Figure 27: Comparison of Hydrogen production in different morphologies of MoS <sub>2</sub> .....	77
Figure 28: Comparison with different sacrificial agent.....	78

## **Chapter 1: Introduction**

Hydrogen is the lightest chemical element and is denoted by the symbol H, with an average atomic weight of 1.00794 amu (1.007825 amu for hydrogen-1), it also has the atomic number 1. It makes up around 75% of the baryonic mass, making it the most prevalent chemical in the universe. Hydrogen is the main element of non-remaining stars when they are in their plasma stage. At room temperature and pressure, hydrogen, a diatomic gas with the chemical formula H<sub>2</sub>, is extremely combustible and devoid of any flavor, color, odor, toxicity, or metallic properties. Since it readily forms covalent compounds with the majority of other elements and is abundant in water and organic compounds, its atomic form is rare on Earth. With several processes requiring the transfer of protons between soluble molecules, hydrogen is essential in acid-base chemistry.

As a safe and useful energy source, hydrogen has the potential to provide important advantages as a green and cost-effective substitute. Its characteristics as a fuel are almost ideal because we can generate it from a lot of ways and convert it into different forms of energy without emitting harmful substances. This reduces the production of greenhouse gases, pollutants that have an impact on certain criteria, and the use of non-renewable energy sources, among other benefits [3]. Due to the potential for materials to store a higher volumetric energy content than compressed hydrogen gas, research in the area of material-based hydrogen generation and storage has drawn a lot of attention.

## 1.1 History

By mixing zinc metal and hydrochloric acid, British scientist Henry Cavendish discovered hydrogen in 1766. The first time hydrogen was utilized as a fuel was in 1783 when French physicist Jacques Alexander Cesar Charles launched a manned hydrogen balloon. Time travel to 1845, when Sir William Grove—also referred to as the "Father of the Fuel Cell"—developed a usable "gas battery" based on the fuel cell effect. NASA employed hydrogen as a source of fuel for different cells and a propellant for their space flights beginning in 1958. Liquid hydrogen was the most common form of hydrogen used commercially.

The University of Miami hosted the first conference which was internationally held on hydrogen energy in 1974 under the name Hydrogen Economy and the Miami Energy Conference (THEME). The attendees, who were engineers and scientists, went on to found the International Association for Hydrogen Energy (IAHE). In 1990, Germany's Solar-Wasserstoff-Bayen became the first hydrogen production facility in the world to be powered entirely by solar energy. The first hydrogen-powered fuel cell vehicle was unveiled by NECAR in 1994, and three hydrogen fuel cell buses were unveiled by the Chicago Transit Authority in 1995. Iceland first put up its aim for a hydrogen economy by 2030 in 1998. In Germany, Hamburg and Munich saw the opening of the first hydrogen filling stations in 1999. Spencer Abraham, then-US Energy Secretary, committed more than \$350 million in financing for initiatives involving hydrogen research and vehicle demonstration in 2004.

## **1.2 Challenges:**

### **1.2.1 Energy Crisis**

An extensive scientific inquiry into environmentally friendly alternative energy sources has been triggered by the rising importance of the energy issue and environmental degradation[1]. Fossil fuels are used to overcome the lot of world energy needs, which presents substantial supply and demand concerns. Additionally, the combustion of these fuels results in the release of poisonous gases including NO<sub>x</sub> and SO<sub>x</sub> as well as dangerous emissions of carbon particles, CO<sub>2</sub>. Affordable and practical renewable energy sources are therefore essential for achieving sustainable global development [2]. The current energy crisis is causing extensive and complex disruptions, particularly in the markets for natural gas, coal, electricity, and oil. To stop additional disruptions, the crisis has prompted IEA member nations to surrender significant amounts of oil reserves. The energy market is still vulnerable to geopolitical and economic uncertainties, and this crisis has brought to light how unstable and unsustainable the current globally system of Energy is according to the Outlook 2022 of the World Energy. According to this year's WEO, stronger policies that can enable a large increase in energy investment must be put in place in order to overcome the dangers of coming time price huge increase and volatility.

### **1.2.2 Present Fuel Options**

The current situation in the world's energy industry appears to be quite difficult, necessitating immediate action to look for other sources of energy generation. The need to

investigate alternative fuel and energy choices has arisen as a result of factors like rising oil prices, uncertainty regarding the ability of oil-producing nations to supply the soaring demand, and declining levels of traditional oil production. Potential alternative fuels include practical alternatives like petrol to liquid, coal to liquid, coal gasification, biofuels, methanol (methanol fuel cell), and gaseous or liquid hydrogen[3]. While some processes have larger environmental disadvantages than others, some produce less greenhouse gas emissions than others. For instance, due to the significant CO<sub>2</sub> emissions it generates, converting hydrogen to methanol is not a practical choice[4].

Fuel alternatives are selected based on things like their high energy density, portability, and distribution infrastructure for storage and transportation that already exists. The advantages and disadvantages of each fuel must be taken into account for certain applications to ensure optimal use. In order to eliminate the necessity for moving fuel and energy from one place to another, it should also be encouraged to produce and use them locally[5]. It is commonly acknowledged that harnessing solar energy to produce eco-friendly hydrogen fuel from water is a highly sustainable strategy for addressing both the world's energy needs and environmental challenges[6].

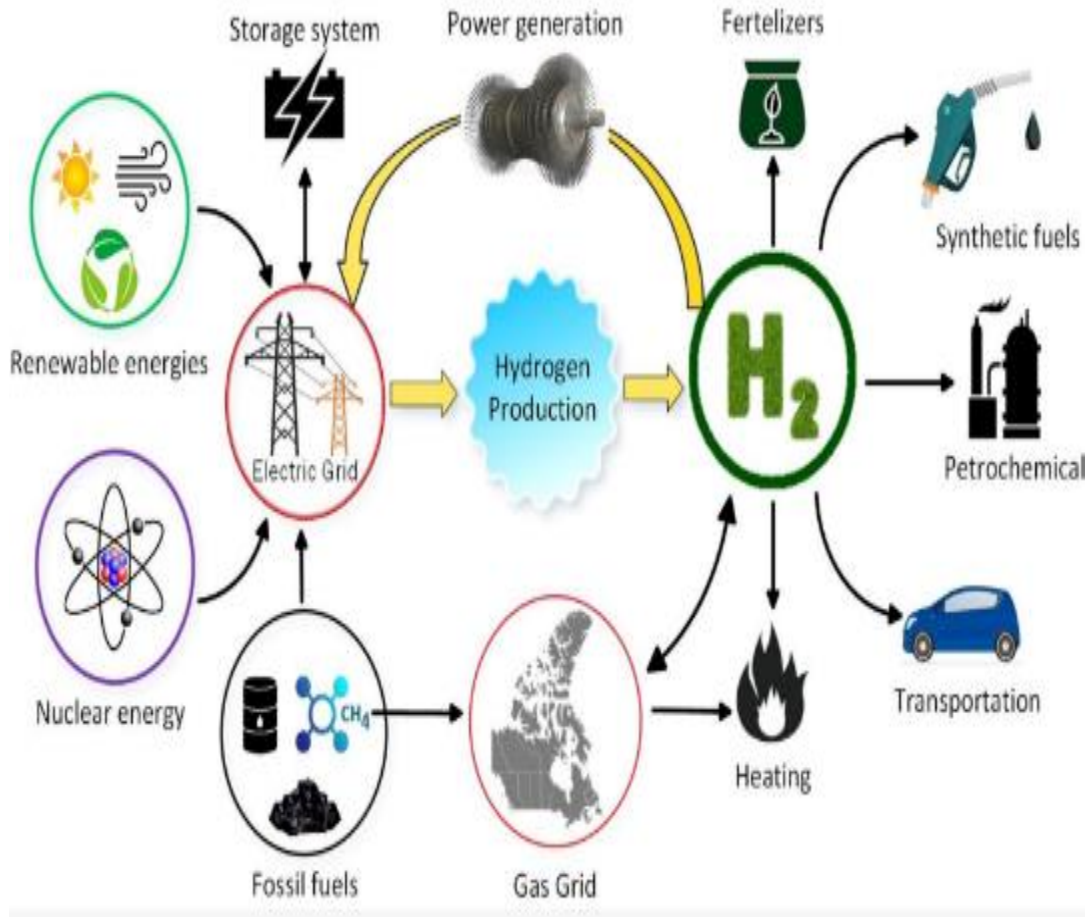


**Figure 1:** Hydrogen be utilized as Energy

Since hydrogen has been generating energy for the sun through fusion reactions for billions of years, it is often regarded as the most effective source of energy. Its biggest strength is that it may be utilized in a variety of applications, including explosives, combustion engines, propellants, and PEM-Fuel Cells, which can generate energy. The hydrogen bomb, which has the ability to destroy the entire world with just three of them, is the biggest bomb ever made, demonstrating its incredible power. In addition, scientists think that understanding hydrogen fusion reactions could offer a limitless answer to the world's energy dilemma.

Currently, the primary emphasis of energy scientists and engineers is investigating hydrogen's potential for usage in PEM-Fuel Cells.

### **1.3 Why Hydrogen?**

The thought behind producing hydrogen as a fuel via various methods is not new. Despite the fact that many nations have long used hydrogen as a source of lighting and heating[3]. Recent advancements in fuel cell technology have reignited facts in hydrogen as a fuel. Due to the fact that a big portion of fossil fuels are utilized for transportation, fuel cells have the potential to save a substantial amount of these non-renewable resources [7, 8]. Hydrogen is a clean fuel, but its environmental advantages depend on how it is produced. It cannot be regarded as environmentally beneficial if it is created using conventional techniques that depend on coal or fossil fuels because CO<sub>2</sub> emissions would have already taken place [4]. Therefore, the method of hydrogen production is crucial, and a clean method should be used to ensure the environmental benefits of hydrogen as a fuel.

### **1.4 Hydrogen as a Fuel**

The high calorific value of hydrogen and the environmentally friendly nature of its reaction byproducts have positioned it as a potential alternative fuel, especially in light of concerns about resource depletion and the environmental implications of using fossil fuels. Despite the increased interest in renewable energy, there are issues with the storage and transportation of hydrogen due



to its low boiling point and poor compressibility [9, 10]. As a result, considerable efforts have focused on discovering in-situ hydrogen generation materials.

### **Approaches for hydrogen production**

- Utilizing fossil fuels
- Renewable resources
- Electrolysis of water,
- The reaction of reactive metals

### **Strategies of hydrogen production**

- **Steam reforming**
- **Thermal cracking**
- **Coal gasification**
- **Electrolysis**
- **Photochemical**
- **Thermal decomposition**

## Hydrogen production processes

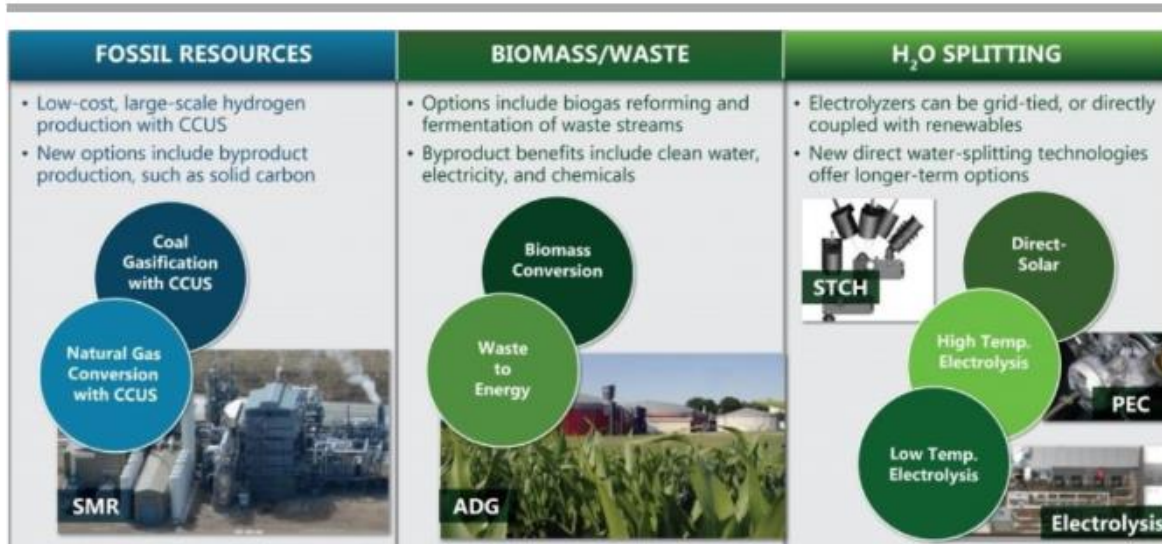
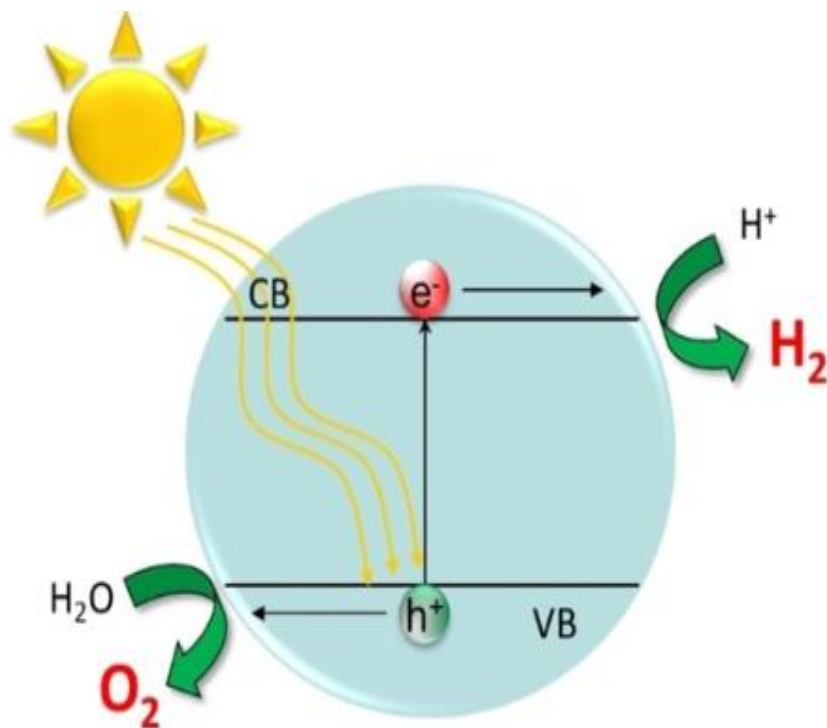


Figure 2: Hydrogen production processes

### 1.5 Photocatalysis

In 1970, the idea of photocatalysis was initially investigated when water was divided into hydrogen utilizing sun and UV light. A new application for environmental cleanup was put forth in 1980.[11] Since then, interest in the potential of this technology for self-cleaning surfaces, hydrogen production, and the purification of water and the air has increased[12]. A type of catalysis known as photocatalysis allows for oxidation-reduction reactions with a variety of uses, such as the purification of water and air. It is also regarded as a sophisticated oxidation process, and in recent years, much research has been done on it. According to the IUPAC (International Union of Pure and Applied Chemistry), "photocatalysis refers to the process of increasing the rate of a photoreaction or starting it by using a catalyst in the presence of light radiation (such as ultraviolet, visible, or infrared) with a semiconductor substance that continuously absorbs light

and interacts to regenerate electrons/holes". Homogeneous or heterogeneous photocatalytic reactions are possible; the latter has received the greatest attention due to its potential for usage in energy and environmental-related applications.



**Figure 3:** Photocatalysis

### 1.5.1 Types of Photocatalysis

- **Homogeneous Catalysis**
- **Heterogeneous Catalysis**

#### **Homogeneous Catalysis**

When the photocatalyst and reactants are present in the same phase, the reaction is referred to as homogeneous photocatalysis. The homogeneous photocatalyst is often ozone or a photo-

Fenton system.[13] This area of research focuses on the degradation of pollutants in water, and producing strong oxidizing species like  $\text{OH}\cdot$  or other radicals is necessary to effectively oxidize organic contaminants. The advanced oxidation process (AOP), which uses transition metal oxides, ozone photolysis, and hydrogen peroxide photodecomposition ( $\text{H}_2\text{O}_2/\text{UV}$ ), is one example of this[14].

### **Heterogeneous Catalysis**

With the liquid or gaseous reactants coming into touch with a solid photocatalyst, heterogeneous photocatalysis refers to a reaction in which the reactants and photocatalyst exist in distinct stages. This photocatalyst is typically composed of a substance that absorbs light and promotes photocatalytic processes at the gas–liquid interface. This method has applications in the fields of environmental science, organic synthesis, and energy [15]. Hazardous organic waste can be converted into less dangerous chemicals by using photocatalysis. Additionally, heterogeneous photocatalysis is a reasonably priced technique for removing pollutants from the environment [16]. The process of classical heterogeneous catalysis can be divided into six distinct stages that operate independently. These stages include

- Transferring reagents from the fluid bulk to the catalyst surface,
- Adsorbing at minimum one reagent,
- Generating an electron/hole charge pair through absorbed photons,

- Reacting in the adsorbed phase,
- Desorbing the resulting products,
- Removing from the catalyst-fluid interface region.

In contrast to conventional catalysis, photocatalytic reactions activate the catalyst through the absorption of photons (step c) as opposed to thermal activation [17].

A reactant and a semiconductor photocatalyst are both present in heterogeneous photocatalysis, although in distinct phases. This enables the photo conversion of diverse chemical entities in both aqueous solutions and the gas phase via a light-induced redox reaction on the semiconductor surface. The first phase in semiconductor photocatalysis is band gap excitation, which happens when light with energy equal to or greater than the band gap excites the valence electrons to the conduction band while the valence holes remain in the semiconducting materials at their initial energy level. The excited holes and the pairs of electron are carried to the material's surface in the second phase, where they interact with absorbed constituents including water, oxygen, or different inorganic or organic compounds in oxidation-reduction reactions. The photocatalytic remediation of water and air is based on these redox processes [18].

Photocatalytic type reaction has two major categories: a) "uphill ( $\Delta G > 0$ ) and b) downhill ( $\Delta G < 0$ ) reactions", as shown in Figure

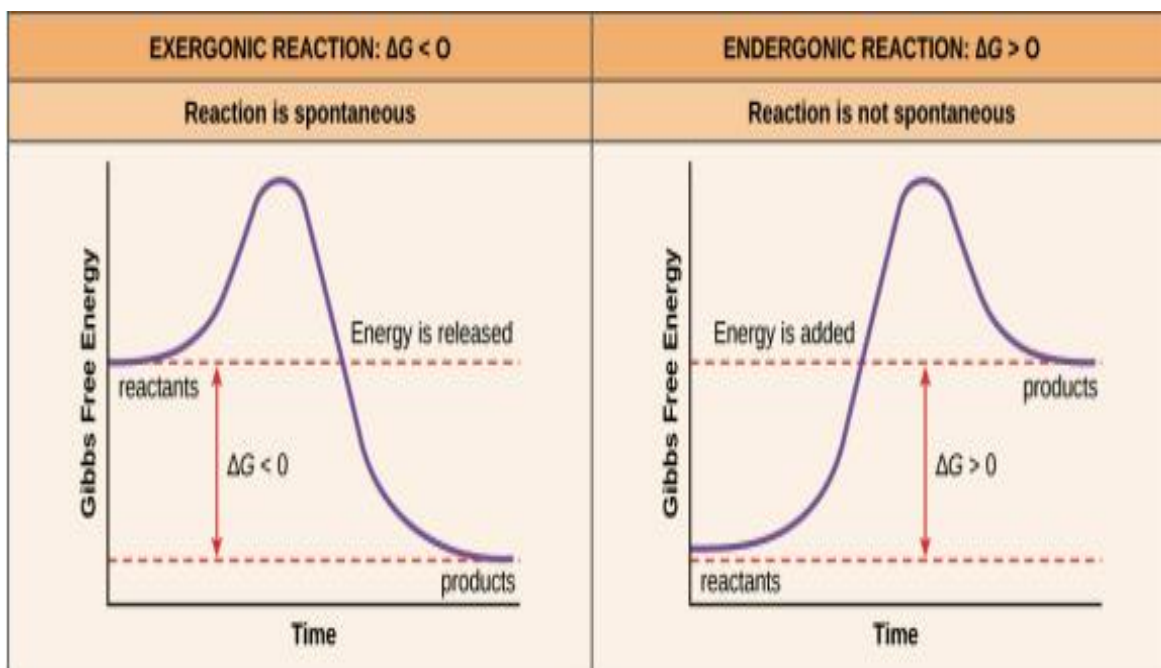


**Figure 4:** Photocatalytic Reactions[19]

Organic pollutants typically degrade by procedures like photo-oxidation using oxygen, which is typically an irreversible reaction with a negative Gibbs free energy ( $G$ ) value, or a reaction going downhill. Titanium dioxide is frequently employed in the investigation of these generated photo reactions. Secondly, water degrades into hydrogen and, oxygen needs a large amount of energy and is an uphill reaction due to its positive  $G$  value of 273 kJ/mole. Similar to photosynthesis in plants, in this process, photon energy is transformed into chemical energy. Because of this, the process of water dissociation is frequently called artificial photosynthesis. The activity associated in the photocatalytic production of  $H_2$  are illustrated in Figure.

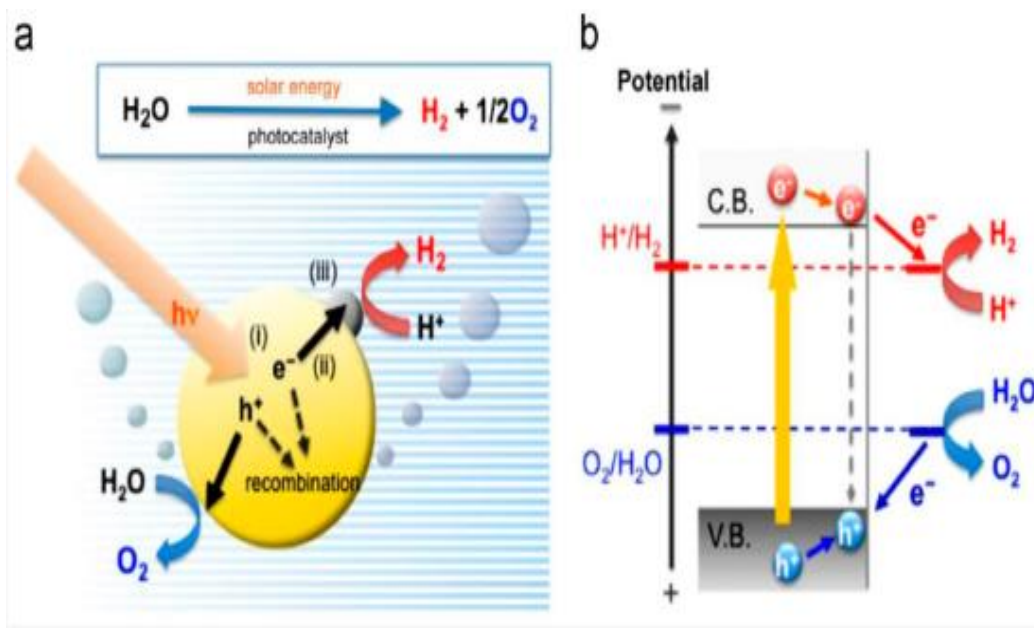
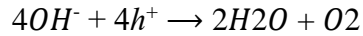


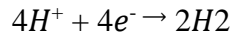
**Figure 5:** Schematic diagram of hydrogen production through water splitting methodology over photocatalysts[20].

When a semiconductor is subjected to photons with greater energies than its energy of the band gap ( $E_{bg}$ ), the photons are absorbed and, in the conduction and valence bands, respectively, two electron charge carriers and vacancies are produced. The accompanying Figure provides an illustration of this procedure. After that, the charge carriers move towards the photocatalysts surface where they can take part in reducing and oxidizing adsorbed water molecules to produce hydrogen molecules [21]. However, there is a risk of competing and unwanted charge carrier recombination, which releases energy in the form of heat or photons [22]. The energy carried by photons can be transformed into the another form of energy which is chemical energy in the form of hydrogen through a process that involves both oxidation and reduction reactions.

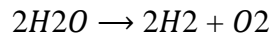
Oxidation:



Reduction:



Overall reaction



A semiconductor's ability to dissociate water depends on its redox potential, which is determined by the disparity in energy between its valence and conduction bands for both reduction type and oxidation type reactions. The electronic design of a potential photocatalyst must satisfy two requirements in order to make H<sub>2</sub> production possible. (i) The band gap must fall between 1.24 eV and 3.26 eV in order to guarantee the desired wavelengths of 1000 nm, and 380 nm. (ii) The highest point of the valence band should be at a work that is more positive than the O<sub>2</sub>/H<sub>2</sub>O redox potential (1.23 V), while the conduction band's lowest point should be at a potential that is more negative than the H<sup>+</sup>/H<sub>2</sub> redox potential (0 V versus NHE at pH=0).

(a) **Recombination by electron and holes produced by light:** Light produces CB electrons and VB holes, however, these particles can quickly combine and release their energy as heat or photons, which is useless for the intended use.



(b) **Competitive backward reaction:** The energy-intensive process of converting water into hydrogen and oxygen renders it vulnerable to a competitive backward reaction that can readily take place and prevent the desired outcome.

(c) **Absorbs only UV light:** Only permits the absorption of UV or near-UV light consists of a relatively small percentage of the solar energy spectrum. TiO<sub>2</sub>, a substance often used for photocatalysis, has a band gap of 3.2 eV. As a result, hydrogen production by photocatalysis is limited. Photogenerated electron/hole pair recombination

### 1.6 Mechanism of Photocatalytic Hydrogen Production

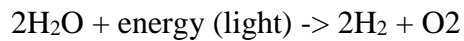
1. In the production of hydrogen process, water is broken down photocatalytically to produce hydrogen gas. A photocatalyst, a substance that can absorb light energy and use it to fuel chemical processes, is used in this procedure.
2. The following actions are commonly taken throughout the photocatalytic hydrogen generation process:
3. **Absorption of light energy:** By absorbing light energy, the photocatalyst stimulates the material's electrons.
4. **4. Production of electron-hole pairs:** The excited electrons go to the photocatalysts conduction band, while the excited holes migrate to the valence band. As a result, the material generates electron-hole pairs.

## 5. **Water oxidation**

Water molecules interact with the photocatalyst holes, causing them to split into oxygen and hydrogen ions.

6. **Hydrogen reduction:** Hydrogen gas is created when the excited electrons in the photocatalysts conduction band interact with the hydrogen ions.

7. Following is a representation of the overall photocatalytic hydrogen generation reaction:



Materials like titanium dioxide (TiO<sub>2</sub>), zinc doped materials and other semiconductors are frequently utilized as photocatalysts in the hydrogen production process. These substances contain a bandgap that enables them to take in light from the visible and UV spectrums. A few of the factors that determine how well photocatalytic hydrogen production functions are the properties of the photocatalyst and characteristics of the light source, and the reaction circumstances.

### **1.6 Photocatalyst Selection for Hydrogen Production**

To efficiently manufacture hydrogen from the photo-dissociation of water, the photocatalyst used must meet specific requirements. The band gap must be suitable for absorbing visible light and initiating water dissociation, first and foremost. Second, it must be able to identify photo excited electrons from photo excited holes. Thirdly, it ought to lessen the energy losses resulting from charge carrier recombination and transfer. It needs to be chemically stable in order

to stop corrosion and photo-corrosion in aquatic environments. The ability to transport enough electrons between water and the catalyst surface should be the fifth need. Finally, it should be easy to synthesize and cheap to produce. The electrical structure of a semiconductor is a crucial factor to consider when trying to develop an effective water dissociation process for photocatalytic hydrogen production. [23].

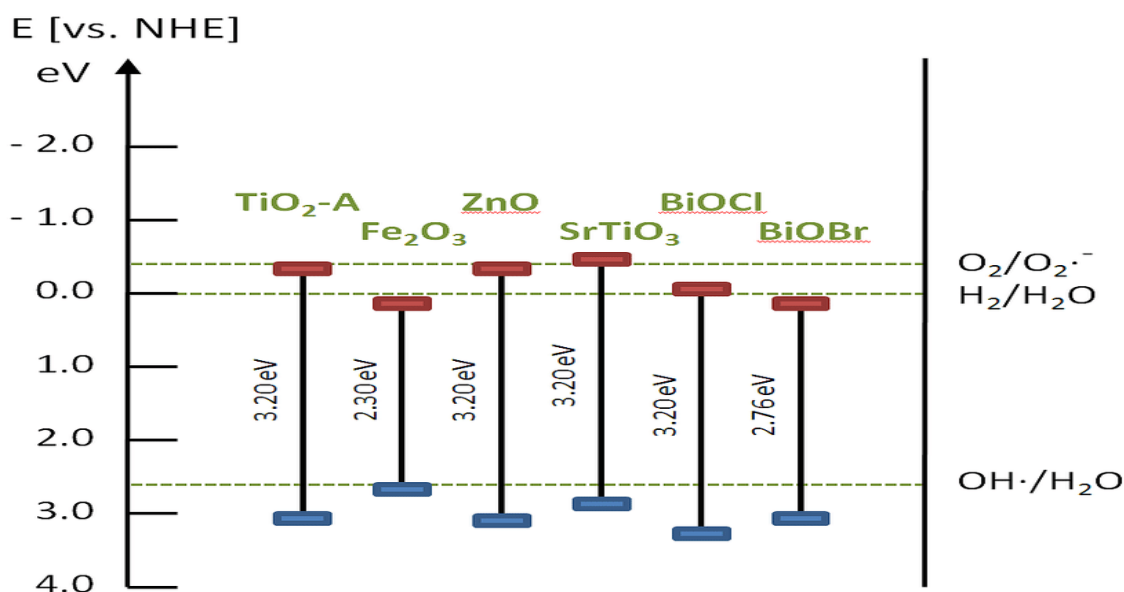


**Figure 6:** Different semiconductor oxides and oxyhalides' band gap energies and band gap edge positions, as well as a few selected redox potentials, are discussed [23].

The semiconductors indicated in Figure are all good semiconductors, but only BiOBr, Fe<sub>2</sub>O<sub>3</sub>, TiO<sub>2</sub>, ZnO, SrTiO<sub>3</sub>, and BiOCl are thermodynamically feasible for water dissociation in the presence of sunshine. Due to its suitable bandgap (2-2.2 eV), which enables absorption of solar

radiation up to 600 nm, the semiconductor  $\text{-Fe}_2\text{O}_3$  is a viable alternative for photocatalytic hydrogen production for the aforementioned reasons. Additionally, it has beneficial qualities like a high photocurrent density, superb stability, low toxicity, and widespread availability in the earth's crust. Therefore, we employ it here to produce hydrogen. Semiconductors need to have energy gaps that are bigger than the theoretical value in order to be acceptable for photocatalytic hydrogen synthesis. This is due to obstacles that currently exist to effectively transfer charges from the photocatalyst to water as well as a propensity for charge carriers to mix[24].

Engineering the photocatalysts microstructure and exterior surface area is crucial for reducing energy losses during the photocatalytic process. Crystallinity and smaller particle size, which lessens grain boundary effects and electron/hole recombination, are both beneficial to the photocatalysts photo activity. The charge carrier diffusion length should be larger than the particle size to enable effective charge transport. The possibility of charge carriers reaching the particle surface rises with decreasing photocatalyst particle size, which is essential for efficient photocatalytic hydrogen production[25].

### **As an good photocatalyst**

Two qualities that a photocatalyst should have.

- i. The capacity to switch to a positive valence state

- ii. Accepting a hole without falling apart.

Hydroxyl radicals are produced by significantly lowering photogenerated electrons and highly oxidizing photogenerated holes. The semiconductor must have at least one stable valence state in order to prevent deterioration from hole formation. Because of the holes, CdS with Cd<sup>2+</sup> and ZnO with Zn<sup>2+</sup> corrode. In addition, the photocatalyst must to be economical, non-toxic, and exceptionally resistant to chemical degradation.

### **1.7 Design to upgrade the photocatalyst efficiency**

Improved photocatalyst efficiency design by Controlling the electrical structure of the material precisely is crucial for producing effective photo catalysts that can function in visible light. Several tactics that fall into three categories can be used to accomplish this

- i. The creation of a composite semiconductor
- ii. Anion or cation doping
- iii. The creation of a semiconductor alloy, and more.

The creation of composite semiconductors by combining several semiconductors is one method for creating an active photocatalyst for visible light. In order to implement this method, two semiconductor qualities must be combined: Semiconductor (a) has a high "forbidden" energy gap, whereas Semiconductor (b) has a tiny "forbidden" energy gap. The "forbidden" energy gap refers to the energy range that electrons cannot occupy in a material. It is conceivable to permit electron

injection from Semiconductor (a)'s more negative conduction band (CB) to Semiconductor (b's CB) by connecting the characteristics of the two semiconductors. This could improve the effectiveness of the photocatalytic method of producing hydrogen.

Combining CdS (with an energy gap of 2.4 eV) and SnO<sub>2</sub> (with an energy gap of 3.5 eV) semiconductor composites, which can utilize visible light irradiation and the sacrificial agent EDTA, could result in the creation of hydrogen [26]. Contrarily, research has shown that using TiO<sub>2</sub> composites combined with a semiconductor that has a "forbidden" energy gap is more productive when exposed to UV radiation [27].

Several requirements must be satisfied for semiconductor composites to be effective in producing hydrogen. First of all, neither semiconductor should corrode from light. Second, it must be feasible to introduce electrons. The semiconductor should, thirdly, respond to visible light. Fourthly, semiconductor (b) must have a lower CB energy level than semiconductor (a). Finally, compared to the decrease level of water, the CB of semiconductor (b) should have a greater negative energy level. Hematite (-Fe<sub>2</sub>O<sub>3</sub>) is the most prevalent and thermodynamically stable type of iron oxides among the aforementioned minerals [28, 29]. It has an indirect band gap with an energy (E<sub>g</sub>) range of 1.91-2.21 eV [30], This shows that it is visible light responsive and becomes active when exposed to wavelengths below 650 nm. However, due to a number of reasons, such as the majority carriers' poor conductivity, -Fe<sub>2</sub>O<sub>3</sub> has a very less quantum efficiency at ambient

temperature [31, 32], a short diffusion length ( $LD = 2-4$  nm) of minority carriers [30], and a small absorption coefficient[33]. When  $\text{-Fe}_2\text{O}_3$  is utilized as a photocatalyst, these restrictions reduce the effectiveness of charge separation, the conversion of visible light energy, and photocatalytic activity.

## **1.8 Heterojunction**

A heterojunction is the boundary or contact between two distinct semiconducting materials with dissimilar band gaps. These interfaces have a substantial impact on the electronic energy bands of solid-state devices, such as transistors, solar cells, and semiconductor lasers. The phrases heterostructure and heterojunction are sometimes used interchangeably to refer to the combination of various heterojunctions within a device. Even so, it is not strictly necessary for the materials to have semiconductors with different band gaps, especially at shorter length scales where spatial characteristics are what determine electrical capabilities.

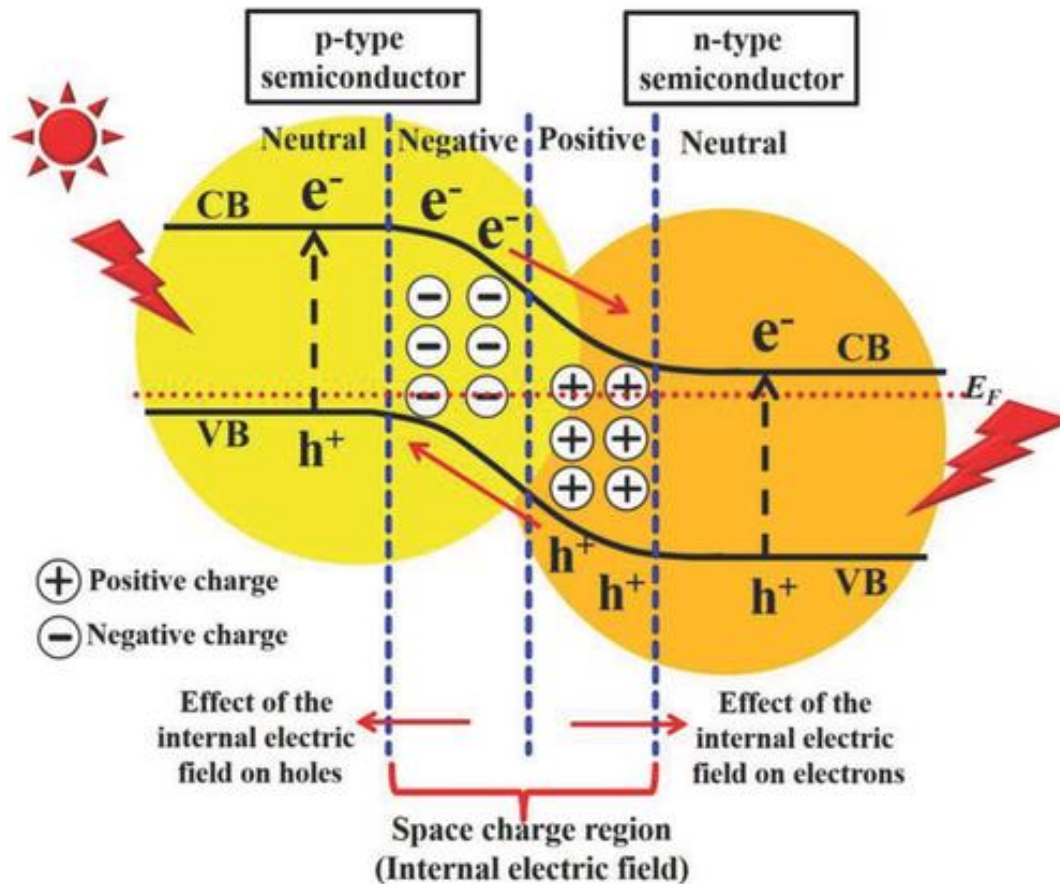


**Figure 7:** Schematic diagram in which we show how electron and holes are separated and how electric field produced and junction between p and n-type photocatalyst

Any interface between solid-state materials, regardless of their crystalline or amorphous structures or their qualities as metallic, insulating, rapid ion conductor, or semiconducting materials, is included in the contemporary concept of a heterojunction.

### 1.9.1 Types of heterojunction

- Type I
- Type II,
- Type III,



- **Z-scheme Heterojunction**
- **S-scheme heterojunction**

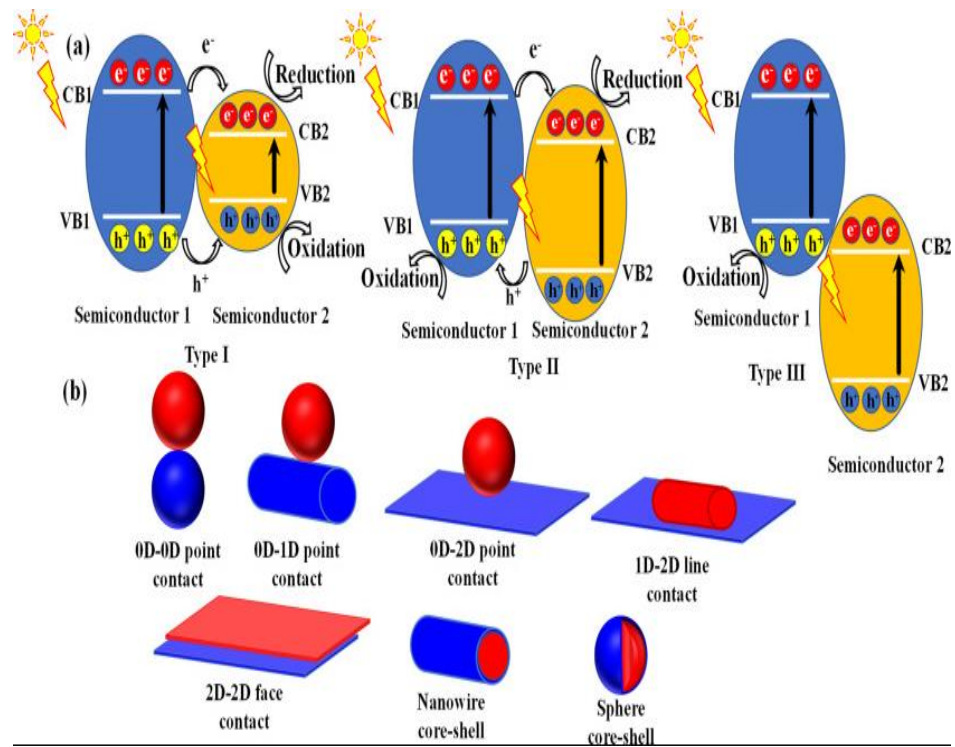


**Figure 8:** A schematic showing various heterojunction photocatalysts: type I, type II, and type III; partial

contact; and core-shell [34].

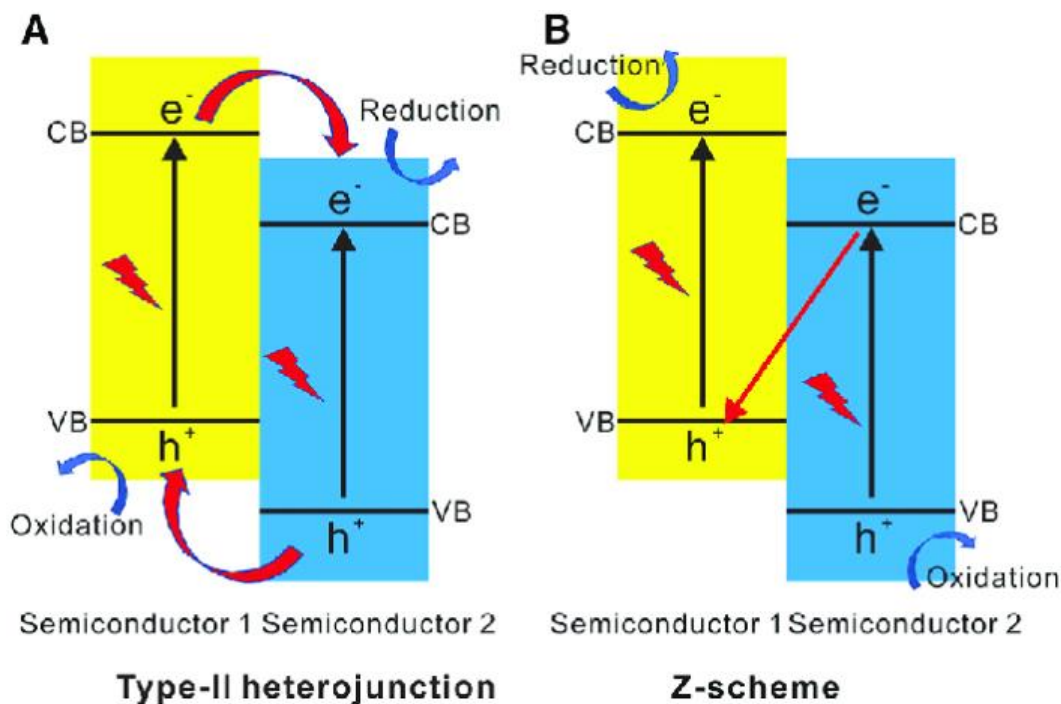


**Figure 9:** Type II heterojunction and Z-scheme photocatalysts' photocatalytic mechanisms Photocatalysts for type II heterojunction [35].

### 1.9 S-scheme heterojunction

We have looked at type-II heterojunction photocatalysts and Z-scheme photocatalysts, the latter of which comprises a range of types and the former of which has significant basic issues. However, the standard Z-scheme photocatalysts have a number of drawbacks, raising concerns about how well their substitutes will work. Direct Z-scheme photocatalysts are likewise impacted by limitations from prior generations. As a result, it is suggested to abandon the words "Z-scheme" and "type-II heterojunction" in favour of a fresh concept that better describes the photocatalytic action. Our team has therefore proposed a scheme which is s-scheme (or Step-scheme) heterojunction as a substitute [36].

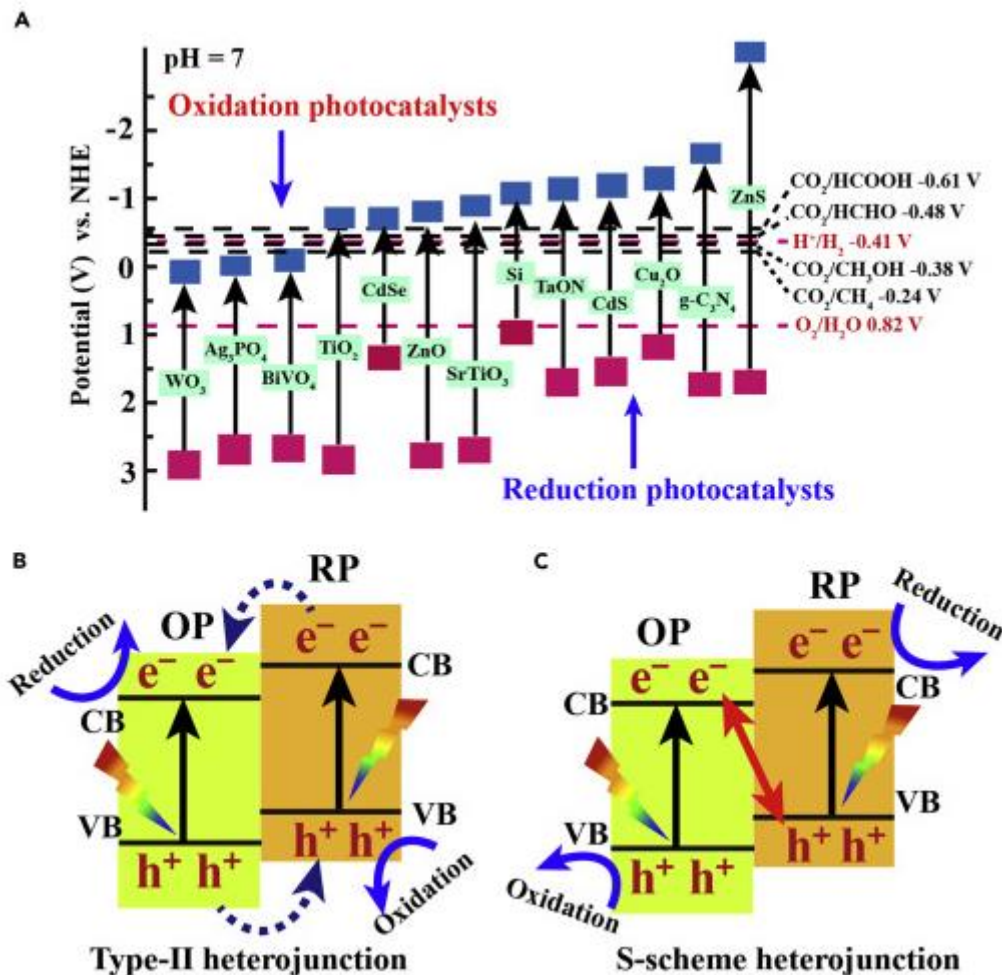


**Figure 10:** Charge Transfer Differences in Type-II and S-Scheme Heterojunctions[37]

Band topologies of a few sample photocatalysts are shown in Figure 10(A).

(B and C) Type II heterojunction and S-scheme heterojunction band structure configurations and charge-transfer paths.

The particular definition will be covered in more detail in the paragraph that follows.

Photocatalysts can be split into two groups: reduction processing photocatalysts (RP) and oxidation carrying photocatalysts (OP), based on their band structures. Strong conduction band (CB) properties of RP make it a popular material for solar fuel production. While photogenerated

electrons are useful in RP, photogenerated holes must be removed using sacrificial agents. But OP's primary goal is to damage the ecosystem. In OP, photogenerated holes provide the energy, whereas photogenerated electrons are useless. It differs from a type-II heterojunction in terms of how charges are transported, and is composed of reducing and Oxidizing potential with staggered band topologies (figures 8b and c). A type-II heterojunction has a limited redox capacity because negatively electrons and positively holes which are produced by light collect on the valence band (Valance Band) of the RP and the Conduction band of the OP, respectively. However, a substantial redox potential is produced in an S-scheme heterojunction where strong photogenerated electrons and holes are stored in the CB of an RP and the VB of an OP, respectively [38, 39]. In the microscopic perspective of the S-scheme mode, the charge-transfer channel is symbolized by the letter N, whereas in the macroscopic view it is represented by a "step" moving electron from lower band to upper band.

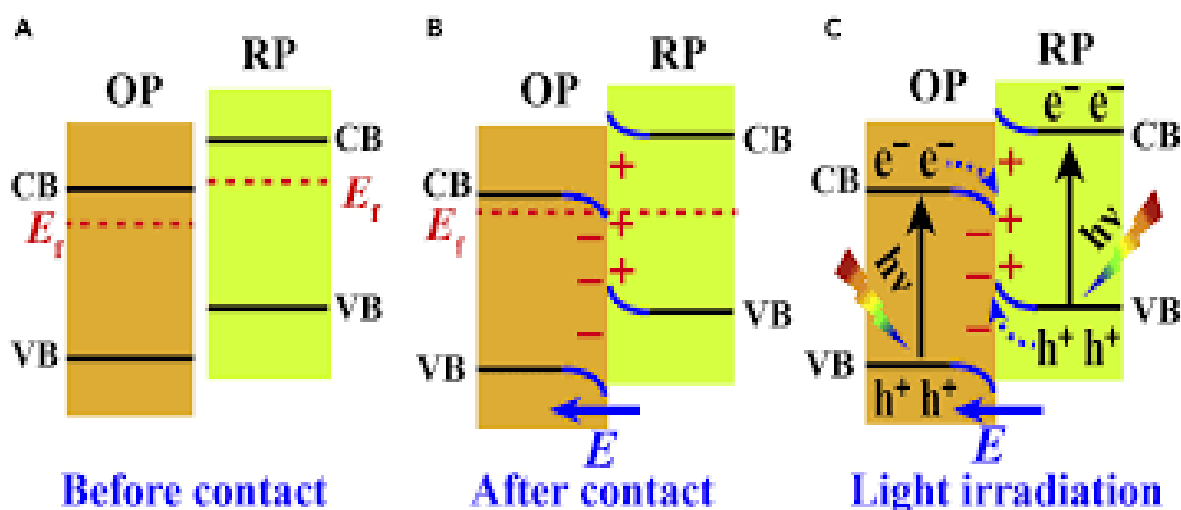


**Figure 11:** S-scheme heterojunction Photocatalyst

Processes of transferring charge in an Step-Scheme Heterojunction (A–C) The light produced charge carrier transfer process in S-scheme mode is shown in (A) before contact, (B) after contact, and (C) in a schematic depiction of a heterojunction with staggered band arrangement.

The mechanism of charge transfer in an S-scheme heterojunction can be described in the following way [40]. The spontaneous diffusion of electrons from the photocatalyst with higher CB and VB positions to the other semiconductor results in the creation of an negatively charge specie depletion layer and an electron accumulation layer at the interface of two semiconductors. When two semiconductors in the CB and VB positions, which have separate work functions, come into close proximity, this happens. (See Figure 10a). The production of an internal electric field between the two semiconductors (Figure 10b) is a second process that aids in the movement of photogenerated electrons from one semiconductor to the other. In Figure 10c. Thirdly, when the Fermi energy levels of the two semiconductors align, band bending and the recombination of photogenerated electrons and holes are triggered at the interface area. This recombination is encouraged by the Coulombic attraction between the electrons and holes. Band bending, Coulombic attraction, and the interaction of the internal electric field all contribute to the recombination of electrons and holes. This method preserves strong photogenerated electrons and holes for photocatalytic reactions while removing wasted carriers [41-44].

## 1.10 Modification

To get beyond  $\text{-Fe}_2\text{O}_3$ 's drawbacks as a photocatalyst, two techniques have been developed: the manufacture of nanostructured iron oxide and the development of ternary and binary material using the S-scheme heterojunction with other semiconductors [29, 45, 46]. Bismuth oxybromide (BiOBr) is a N-type semiconductor with a band gap energy of 2.710 eV [47]. It has been used with other metal oxides to make composites that have better visible-light photocatalytic activity[48, 49]. This suggests that composites of BiOBr and  $\text{-Fe}_2\text{O}_3$  may also exhibit strong light produced activity when these are present to visible light. Bismuth oxybromide (BiOBr), the focus of this study, exemplifies how oxygen vacancies (OV) can dramatically quicken the separation of excitons, leading to a larger output of charge carriers. It is found that the faulty BiOBr with OV performs very well in photocatalytic reactions involving charge carriers, such as the creation of superoxide and the coupling of amines via aerobic oxidation. This study sheds light on the application of defect engineering to the development of better photocatalysts [50].

In this study,  $\text{-Fe}_2\text{O}_3$  and BiOBr were combined to create composites for the synthesis of hydrogen utilizing a novel approach. In comparison to earlier research that employed a solvothermal approach with EG as the solvent, the method, which involved a hydrothermal procedure, was found to be more simple, affordable, and environmentally benign [51][52]. The composites' capacity to create hydrogen when exposed to visible light was used to assess its photocatalytic properties.

By creating a junction between n-type Bismuth oxybromide and n-type alpha iron oxide semiconductors, photoinduced electron-hole pairs can be separated. By using an magnetic field which is developed externally, superparamagnetic BiOBr/Fe<sub>2</sub>O<sub>3</sub> composites can also be used for practical separation, and they have shown encouraging results in the production of H<sub>2</sub> through water splitting. Spatial charge separation is enhanced by forming a two-dimensional heterostructure with BiOBr and Fe<sub>2</sub>O<sub>3</sub>, resulting in mmolh<sup>-1</sup>g<sup>-1</sup> H<sub>2</sub> is 57 mmolh<sup>-1</sup>g<sup>-1</sup> at 420 nm, surpassing the AQY of pristine iron oxide and bismuth oxybromide. The active site in this photocatalytic system is the oxygen-vacancy-rich BiOBr, and the photosensitizer is Fe<sub>2</sub>O<sub>3</sub>, leading to an AQY for H<sub>2</sub> production at 420 nm. To our knowledge, this is the first successful attempt at constructing BiOBr/Fe<sub>2</sub>O<sub>3</sub> heterostructures for the purpose of H<sub>2</sub> production.

It is generally known that combining different metals can improve the catalytic activity of metal oxides which belongs to transition metals (TMOs). Bimetallic oxides have been found to be more effective than monometallic oxides, especially in hydrogen evolution processes (HERs). The synergistic interaction of the metal species accounts for the significantly increased HER activity of tri-metallic oxides. This effect is assumed to be a result of electrical structural modification.

### **1.10.1 Modification of band locations of the semiconductor**

Band structure engineering involves manipulating the band positions of semiconductor photocatalytic materials to enhance their utilization of solar energy, thereby improving their efficiency in dye degradation. Here are a few illustrations of band gap engineering techniques.

## **A. Phenomenon of quantum confinement**

A single photon can be used to create many electrons, and quantum confined semiconductor materials have strong photostability, a long excitation lifetime, a higher extinction coefficient, and other beneficial properties. Due to these characteristics, quantum bound nanomaterials are very effective in using solar radiation to degrade dyes. TiO<sub>2</sub> nanoparticles' yield is improved by particle size reduction, especially for CH<sub>3</sub>OH and CH<sub>4</sub>, according to research. Particle size is influenced by the rivalry between charge-carrier dynamics, light absorption effectiveness, and specific surface area. A nanocomposite of graphene oxide (GO) and yttrium with a nanoflake structure was described by Zhang et al. A greater photocurrent density was produced as a result of the presence of GO acting as an electron conductor in Y<sub>2</sub>O<sub>3</sub>. This material exhibited excellent effectiveness in the photocatalytic degradation of methylene blue [53]. Luca et al. conducted the photodegradation of methylene blue using a quantum restricted titanosilicate semiconductor [54]. A graphene oxide-TiO<sub>2</sub> nanocomposite was created by Posa and his coworkers, and it formed particles with an average size of 3-6 nm and had exceptional effectiveness in the photocatalytic destruction of Rh-B dye [55].

## **B. Doping semiconductors**

The efficiency of semiconductors can be high by doping them with either a semiconductor or a noble metal. The band gap of metal oxide semiconductors, which is typically approximately 3 eV, reduces their usefulness as visible light-emitting diodes (LEDs). Doping the semiconductor,



on the other hand, can shrink the band gap, enabling it to emit visible light. Doping is the process of removing partial oxygen from metal oxides and raising the valence band maxima by using anions like carbon (C) and nitrogen (N). Studies have revealed that nitrogen doping reduced the band gap and caused visible-light photodegradation of RNO dye in mesoporous TiO<sub>2</sub> with Ag [56]. Similar to this, Thota et al. described a Titania matrix with nitrogen and manganese dopants that enhanced visible light responsiveness and quantum yield while also reducing recombination by trapping electrons. The band gap caused by doping was reduced as a result of both nitrogen and manganese doping. To increase the effectiveness of UV-active semiconductor photocatalysts, cationic doping is used. The production of diffuse d states by cation doping, however, can result in an increase in recombination centers. Because it makes it easier for electrons and holes to move to the surfaces of the nanoparticles, nickel and copper-doped ZnS has been found to be effective for the photodegradation of organic dyes [57]. Due to the ability of doping to move the absorption edge to longer wavelengths, co-doped ZnO nanoparticles have demonstrated improved photocatalytic efficiency in the degradation of methyl orange. In conclusion, doping encourages charge carrier migration, which changes the properties of charge transfer and enhances photocatalyst performance.

### **C. Solid Solution**

A solid solution of (GaN)<sub>1-x</sub>(ZnO)<sub>x</sub> with a tunable band-gap varying from 2.38 to 2.76 eV was described by Wu et al. This solid solution showed much greater efficiency when compared

to conventional single-component solid solutions. It was discovered that environmental pollutants degraded astonishingly quickly using photocatalysis. The solid solution's improved redox potential and decreased lattice deformation were credited as being key factors in the process that allowed it to successfully breakdown contaminants [58].

#### **D. Heterostructures formation**

Charge transfer rates can be increased and photocatalytic efficacy can be greatly improved by the development of heterostructures. Recombination in semiconductor heterostructures of type II can be avoided by moving holes from the lower valence band to the higher valence band and electrons from the upper conduction band to the lower conduction band. Metal semiconductor heterostructures are often used to separate electrons and holes. Visible light can be absorbed when gold (Au) is linked with a semiconductor with a low band gap. Electron delocalization is caused by interactions between excited semiconductor states and plasmonic gold levels [59]. Numerous applications, including as water splitting and photocatalytic dye degradation, have shown the applicability of such tiny heterostructures. For instance, Nguyen et al. created a  $\text{ZnFe}_2\text{O}_4\text{-TiO}_2$  photocatalyst that produced a Schottky barrier and had particle sizes of 8–9 nm. This barrier significantly slowed down electron-hole recombination and enhanced the photodegradation of dyes like methyl red and rhodamine B (Rh-B) [60].

Similar to this, Min et al. created a nanocomposite of  $\text{BiVO}_4$  and  $\text{TiO}_2$ , which showed improved photocatalytic activity. Charge transfer from  $\text{BiVO}_4$  to  $\text{TiO}_2$  took place in this

heterostructure, increasing  $\text{TiO}_2$ 's sensitivity to visible light and speeding up the photodegradation of dyes. The  $\text{InVO}_4/\text{TiO}_2$  nanostructures are another illustration, which showed efficient photocatalytic destruction of dyes with a low recombination rate [61]. In summary, heterostructures effectively separate charges, leading to increased photocatalytic breakdown of dyes like Rhodamine B.

### **E. Sensitization of semiconductors**

Sensitization of Semiconductors involves fusing a semiconductor with an alternative substance, often one with a wider band gap, to boost the photocatalytic efficiency of the semiconductor which is produced by light of sun. This is important because most metal oxide photocatalysts, such titanium dioxide ( $\text{TiO}_2$ ), work best when exposed to ultraviolet (UV) light, which makes up only a small portion (4%) of the solar spectrum.

To use visible light for photocatalysis, sensitization is used. This method uses a "sensitizer" substance to "sensitize" the semiconductor with the wider band gap, which could be a dye molecule or a semiconductor with a narrower band gap. The sensitizer absorbs visible light, and after that, it moves the photogenerated electrons to the semiconductor's conduction band where they take part in photocatalytic processes. For instance,  $\text{TiO}_2$ , with its wide band gap, is widely used as a sensitising material to enhance the photocatalytic properties of semiconductors with narrower band gaps, such as CdS (cadmium sulphide), PbS (lead sulphide), and CdSe (cadmium selenide). When

combined with TiO<sub>2</sub>, these semiconductors with tiny band gaps can effectively exploit visible light for photocatalysis.

Makama A. B. asserts that the creation of a CdS/TiO<sub>2</sub> nanocomposite demonstrated the degradation of methylene blue under visible light. The sensitizer (CdS) transfers the photogenerated electrons to TiO<sub>2</sub>, which lessens the possibility of charge like electron recombination to the holes generating by light and increases the photocatalytic effectiveness of the nanocomposite. Similarly, photocatalytic degradation of the dye rhodamine blue has been accomplished using g-C<sub>3</sub>N<sub>4</sub>/TiO<sub>2</sub> nanocomposites. At the ideal concentration of g-C<sub>3</sub>N<sub>4</sub> added as a sensitizer, the excited electron lifetime rose from 2.65 to 10.20 nanoseconds, demonstrating effective charge separation and enhanced photocatalytic efficacy. Overall, by improving their capacity to produce and separate photo-generated charge carriers, sensitized semiconductors enable the use of visible light in photocatalytic processes, resulting in increased efficacy in the degradation of pollutants or the facilitation of other desired chemical reactions.

### **1.11 Composing Nano-scale Catalyst**

1. Changing the characteristics of materials at the nanoscale to increase their catalytic activity is a key component in designing nanoscale catalysts. The sentence you gave highlights a number of elements that can have an impact on how well nanomaterials operate as photocatalysts. Here are some factors to take into account while building nanoscale catalysts with enhanced photocatalytic activity, based on the information provided:

2. Single crystal nanomaterials: Due to the lack of surface imperfections and grain boundaries, single crystal nanomaterials like Nano belts, Nanotubes, and Nanowires exhibit better photocatalytic activity than polycrystalline materials. As a result, choosing and creating nanomaterials with single crystal structures can improve the performance of photocatalysis.
3. Charge separation: Charges can be transported directly via one-dimensional nanoparticles, which effectively separates them. The separation of photogenerated charge carriers and prevention of their recombination can be improved by designing nanoscale catalysts with one-dimensional structures, which is advantageous for photocatalytic reactions.
4. Crystal quality and defects: The efficacy of the photocatalytic reaction may suffer from crystal structural flaws. Therefore, efforts should be undertaken to reduce flaws and enhance the catalysts' crystal quality at the nanoscale. To decrease flaws and improve catalytic efficiency, strategies such as precise synthesis procedures, doping, and surface engineering can be used.
5. Particle size: The photocatalytic activity of a photocatalyst is directly influenced by its size. The surface area and the number of sites open to photolytic processes rise as particle size decreases. Therefore, increasing the catalytic surface area of nanoscale catalysts with lower particle sizes can result in increased photocatalytic activity.
6. Band-gap engineering: A semiconductor material's band-gap is a key factor in determining how effective it is as a photocatalyst. The band-gap can be changed to improve light absorption

and encourage effective charge transfer. You may customize the band-gap to maximize photocatalytic performance by choosing the right nanoscale catalyst materials and changing their composition or structure.

7. **Surface area enhancement:** Increasing the exposed surface area of the catalyst can provide more active sites for photocatalytic reactions. Strategies such as designing nanostructures with high aspect ratios (e.g., nanotubes or nanowires) or incorporating nanostructures into thin films can maximize the surface area and improve photocatalytic activity.
8. **Synergistic effects:** When paired with other substances or structures, some nanoscale catalysts may show synergistic effects. For instance, it has been demonstrated that adding Si nanostructures to a titanium dioxide layer dramatically accelerates the photodegradation of organic colors. Enhancing the synergistic interactions between several nanomaterials can enhance catalytic performance.

Defect density is inversely correlated with the quality of the crystal structure, and a high defect density can reduce the photocatalytic efficiency. Additionally, the photocatalysts size influences its photocatalytic activity. The surface area and quantity of reactive sites on the surface increase as the particle size decreases, boosting photolytic reactions [62]. Feng et al. successfully synthesized one-dimensional TiO<sub>2</sub> nanostructures nanotubes, nanowires, and nanobelts are that display extraordinary photocatalytic dye degradation because of their increased surface area, lower

electron-hole recombination, and narrower band gap [63]. Souderi et al. produced thin films of  $\text{TiO}_2$  with a larger exposed surface area by incorporating Si nanostructures, resulting in a 12-fold higher photodegradation rate of methyl orange and methylene blue compared to a flat  $\text{TiO}_2$  film[64]. Additionally, during UV light exposure, the photocatalytic activity of bulk and nano-sized  $\text{Bi}_4\text{NbO}_8\text{Cl}$  was investigated. Compared to earlier research, nano  $\text{Bi}_4\text{NbO}_8\text{Cl}$  showed that Congo red degraded more quickly [65].

In summary, it is important to carefully address issues such crystal structure, defect management, particle size, band-gap engineering, surface area augmentation, and potential synergistic effects when building nanoscale catalysts with increased photocatalytic activity. Researchers can use these elements to create very effective nanoscale catalysts for various photocatalytic applications.

## Chapter 2: Literature Review

Hydrogen is not a naturally occurring substance like fossil fuels are. It is a plentiful renewable energy source, nevertheless. Pure 100% hydrogen can be synthesized by the water splitting process, which separates water into hydrogen and oxygen. Given that the solar energy collected by the Earth in just one hour exceeds the present global yearly energy consumption, it is crucial to capture solar energy through photocatalysis to make hydrogen through water splitting. The method of increasing photoreactions with catalysts is known as photocatalysis. In this procedure, new compounds are formed as a result of interactions between chemical molecules and the electron-hole pairs (e-h<sup>+</sup>) produced by electromagnetic excitation of the photocatalyst. In the 1970s, a significant development in the study of heterogeneous photocatalysis was made when it was shown that a semiconductor-based electrode built of TiO<sub>2</sub> could effectively split water when exposed to UV light [66].

Since then, there has been significant growth in research on heterogeneous photocatalysis, focusing on various applications such as fuel generation through H<sub>2</sub> evolution and CO<sub>2</sub> reduction[67, 68], water and air purification[69], and value-added organic synthesis[70]. During this time, scientists have developed a wide range of photocatalyst materials, including metal oxides (such as TiO<sub>2</sub>, ZnO, and Fe<sub>2</sub>O<sub>3</sub>)[71, 72], sulfides (such as CdS and MoS<sub>2</sub>)[72], and nitrides (such as Ta<sub>3</sub>N<sub>5</sub> and C<sub>3</sub>N<sub>4</sub>)[73, 74], to cater to the aforementioned applications.



Three phases are commonly involved in heterogeneous catalytic reactions: reactant adsorption (which can happen via physisorption or chemisorption), following surface reactions, and product desorption [75]. In the context of photocatalysis, these processes can be separated into two groups: surface reactions and the adsorption, dissociation, and desorption of molecules. In the early stage of a photocatalytic system, the reactant molecules are activated by their chemisorption onto the photocatalysts, which results in the catalysts and reactant molecules forging strong chemical bonds. Desorption of the products from the photocatalysts, on the other hand, results in the catalysts releasing new active sites in the last step. As a result, each of these key processes must be carefully optimized in order to produce highly active photocatalysts for hydrogen (H<sub>2</sub>) evolution and water splitting.

According to Shahid et al it is described how numerous metal oxides, metal sulphides, and metal carbides can produce hydrogen through water splitting. One of the most well-known and practical catalysts for the creation of hydrogen is TiO<sub>2</sub>. The L-Cys capped Nickel cobalt phosphide composite showed an H<sub>2</sub> evolution rate of 218 mmol g<sup>-1</sup> h<sup>-1</sup> and a very high apparent quantum yield of 76.3% at 420 nm. [76] According to Ziwei et al., when exposed to visible light, the Fe<sub>2</sub>P-CdS combination demonstrates excellent photocatalytic activity. A physical mixture of Fe<sub>2</sub>P nanoparticles (NPs) and CdS nanosheets (NSs) exhibits a surprising ability to generate a high quantum yield of photocatalytic hydrogen generation, reaching up to 90% when exposed to monochromatic light with a wavelength of 420 nm. During this productive process, which occurs

in highly alkaline conditions, ethanol serves as the electron donor. In the hybrid photocatalyst system, free-standing Fe<sub>2</sub>P NPs are used as effective and long-lasting co-catalysts, and ultrathin CdS NSs act as photosensitizer. Here, H<sub>2</sub> evolves at a phenomenal quantum yield of 90% at 420 nm and a rate of 220 mmol g<sup>-1</sup> (cat) h<sup>-1</sup> [77].

According to Kebin et al., it is successful to gradually separate MoS<sub>2</sub> nanocrystals into fewer layers by employing photocatalytic water splitting to produce hydrogen bubbles. These few-layered MoS<sub>2</sub> nanocrystals can be combined with CdS nanosheets to form van der Waals heterostructures, more precisely few-layered MoS<sub>2</sub>/CdS nanosheets. This structure effectively promotes the separation and transfer of charges, which considerably increases the photocatalytic activity for hydrogen production. The few-layered MoS<sub>2</sub>/CdS heterostructures exhibit a remarkable hydrogen evolution rate of 140 mmol h<sup>-1</sup> g<sup>-1</sup> and achieve an apparent quantum yield of 66% at a wavelength of 420 nm [78].

According to Cheng et al., a composite material called FeP/CdS, which is made up of FeP nanoparticles and CdS nanocrystals, has been used to create hydrogen (H<sub>2</sub>) in an aqueous lactic acid solution under visible light. Their results show the remarkable activity of this photocatalyst, with an initial H<sub>2</sub>-evolution rate of 202,000 mol h<sup>-1</sup> g<sup>-1</sup> for the first 5 hours (106,000 mol h<sup>-1</sup> g<sup>-1</sup> under natural sun irradiation). Additionally, the FeP/CdS photocatalyst has an apparent quantum efficiency of about 35% at 520 nm [79]. CoP and CdS hybrid catalysts were successfully coupled

in water under solar radiation to create a unique and trustworthy photocatalytic system for hydrogen production, according to Shuang Cao et al. The system demonstrates exceptional robustness and effectiveness. The rate of H<sub>2</sub> production, which astoundingly reaches an incredible 254,000 mol h<sup>-1</sup> g<sup>-1</sup> over a 4.5-hour period of sunlight exposure and exhibits an apparent quantum efficiency of up to 75%, is one of the most remarkable results for CdS photocatalytic systems documented in the literature [80]. An inventive MoS<sub>2</sub>/ZnIn<sub>2</sub>S<sub>4</sub> photocatalyst system that successfully produces hydrogen (H<sub>2</sub>) from visible light (wavelength higher than 420 nm) was described by Guoping et al. The system was created by hydrothermally synthesizing ZnIn<sub>2</sub>S<sub>4</sub> microspheres, followed by a simple photo-assisted deposition process to deposit MoS<sub>2</sub> as a co-catalyst. The photocatalytic activity of H<sub>2</sub> evolution is significantly influenced by the quantity of MoS<sub>2</sub> co-catalyst loaded and the deposition method. Unexpectedly, an H<sub>2</sub> evolution rate of 8.047 mmol h<sup>-1</sup> g<sup>-1</sup> was achieved, which is 28 times higher than that of untreated ZnIn<sub>2</sub>S<sub>4</sub>. [81]. Jia et al., Reported a straightforward in situ growth procedure was used to produce a CdS/GD heterojunction by adding Cd (AcO)<sub>2</sub> to a dimethyl sulfoxide (DMSO) solution containing GD substrate. When compared to pure GD and CdS nanoparticles, the resulting CdS/GD heterojunction exhibits noticeably better photocatalytic hydrogen evolution capability. In particular, the CdS/GD heterostructure containing 2.5 wt% of GD (GD2.5) has 2.6 times the photocatalytic activity of pure CdS nanoparticles. The development of the CdS/GD heterojunction, where GD works as a material for effectively separating photogenerated electron-hole pairs in CdS

and stabilizes the CdS nanoparticles by inhibiting their aggregation, is responsible for the increased catalytic performance [82]. According to Quanjun et al., a novel ternary composite was made using graphene-based materials, most notably CdS nanorods grown atop a hierarchically stacked WS<sub>2</sub>/graphene hybrid (WG). This combination works remarkably effectively as a photocatalyst for the production of hydrogen when exposed to visible light.

The optimal composition of stacked WG in the CdS/WS<sub>2</sub>/graphene composites was determined to be 4.2 wt%, with a hydrogen generation rate of 1842 mol h<sup>-1</sup> g<sup>-1</sup> under visible light at 420 nm and an apparent quantum efficiency of 21.2%. This remarkable photocatalytic activity is achieved by the deposition of CdS nanorods on stacked WS<sub>2</sub>/graphene sheets, which successfully inhibits charge recombination, improves interfacial charge transfer, and provides active sites for reduction activities. The proposed mechanism for the increased photocatalytic activity of CdS nanorods treated with hierarchically stacked WG is further supported by transient photocurrent response experiments. According to this study, a hybrid of hierarchically stacked WS<sub>2</sub> and graphene nanosheets that lacks noble metals has the potential to be a powerful co-catalyst for photocatalytic water splitting [83].

Peifang et al. developed a novel technique to produce composite nanorods of CoP-modified CdS and g-C<sub>3</sub>N<sub>4</sub> via heterojunction engineering and co-catalyst modification. The obtained CoP-CdS/g-C<sub>3</sub>N<sub>4</sub> composites display excellent stability and outstanding photocatalytic performance

when utilized as a photocatalyst for water reduction. It is noteworthy that the rate of H<sub>2</sub> production reaches 23,536 mol g<sup>-1</sup>h<sup>-1</sup>, which is astounding given that it is approximately 14 times greater than that achieved by pure CdS alone. These components helped the CoP-CdS/g-C<sub>3</sub>N<sub>4</sub> composites work exceptionally well: (1) the close closeness of CdS and g-C<sub>3</sub>N<sub>4</sub> improves the separation of electron-hole pairs. (2) CoP is included as a co-catalyst in the CdS/g-C<sub>3</sub>N<sub>4</sub> nanorods,, which improves the removal of photogenerated electrons from the material and lowers the overpotential needed for H<sup>+</sup> reduction [84].

Jianqi et al., Reported a composite of hollow TiO<sub>2</sub>-ZrO<sub>2</sub> spheres produced using a water bath and calcining as a post-processing method. With the unique hollow structure and the addition of TiO<sub>2</sub> and ZrO<sub>2</sub>, the photocatalytic activity is significantly improved. When exposed to UV radiation and artificial sunlight, these TiO<sub>2</sub>-ZrO<sub>2</sub> hollow spheres have excellent photocatalytic capabilities. They also show some ability to produce hydrogen, as shown by the formation of 23.7 mol of H<sub>2</sub> during an 8-hour period by water photolysis [85].

## Chapter 3: Experimental

### 3.1 Synthesis

Here, we synthesize our all target compounds via hydrothermal method but there binary and ternary composite synthesized by solvothermal method.

### 3.2 Required precursors

In this experimental study all compounds, which are used for hydrogen production were synthesized by a series of chemical reagents. In all our experiments distilled water used. First we synthesize  $\alpha$ -Fe<sub>2</sub>O<sub>3</sub>, for this we take FeCl<sub>3</sub>.6H<sub>2</sub>O obtained from Sigma Aldrich as a source of Fe (iron). Ammonium sulfate obtained from-- and trimethylamine amine obtained from Multi Linkx are pivotal material for the synthesis of required product. After this we move toward BiOBr synthesis, for this we use anhydrous Bi (NO<sub>3</sub>)<sub>3</sub> obtained from F.A traders as a source of bismuth. Additionally we KBr from Sigma Aldrich as Br source. Here we also use acetic acid taken from Sigma Aldrich as an essential element to obtained desired texture of product. Our third and most important material is MoS<sub>2</sub>, used as co-catalyst. However chemicals used for this are ammonium molybdate and sulfur powder from Sigma Aldrich. All of the chemical reagents that were purchased and utilized were of analytical grade and did not require any additional purification. The successful synthesis of the target compound for the hydrogen production was made possible by the combination of these chemicals, which proved to be crucial for the completion of the process.

### 3.3 Synthesis of $\alpha$ -Fe<sub>2</sub>O<sub>3</sub> nanosheets

We synthesize  $\alpha$ -Fe<sub>2</sub>O<sub>3</sub> nanosheets by hydrothermal method. First we take 10ml of de-ionized water in a beaker. Then we weighed 1.00 mmol of iron chloride hexahydrate and 0.256 mmol of aluminum sulfate on the glazed paper and dissolved in the de-ionized water with the help of continuous magnetic stirring to form a transparent solution. Then we add 3ml of triethylamine dropwise in this transparent solution and remain on stirring this solution for 20 minutes more. Then we put this solution in Teflon-lined autoclave (capacity 50ml) and seal it properly. Then we preheat an oven on 160 °C and place autoclave in it for 24 hours[86].

As soon as the reaction was proceeded, the autoclave was left to cool down on its own. The red precipitates settle at the bottom of autoclave were synthesized to collect and centrifuge it at 8000rpm for 8 minutes. This solid product washed with pure distilled water and ethanol. Then we dried this product in the vacuum oven for overnight at 60°C. After this process we achieve a red color nanocrystal of  $\alpha$ -Fe<sub>2</sub>O<sub>3</sub>. To obtain crystal facet of  $\alpha$ -Fe<sub>2</sub>O<sub>3</sub> we calcine this powder in the muffle furnace at 480°C for the 6 hours in a ceramic made crucible without lid covering. After 6 hours we archive our desired product. The synthesis approach outlined in this study aligns with the existing body of literature in the field, where the one-pot synthesis method is frequently employed for  $\alpha$ -Fe<sub>2</sub>O<sub>3</sub> synthesis. Nevertheless, there may be variations in the specific ramping rate and calcination temperature utilized in this study compared to the literature. Fine-tuning the

synthesis conditions, including optimizing the calcination temperature and ramping rate, has the potential to yield  $\alpha$ -Fe<sub>2</sub>O<sub>3</sub> with enhanced properties and higher quality.

### **3.4 Synthesis of BiOBr**

In a typical procedure by which we synthesize the sheets of BiOBr, first of all we weighed 0.243 g of bismuth nitrate on glaze paper and dissolved in the 0.75ml of acetic acid. The resulting solution was then combined with 7.5 mL of de-ionized water containing 0.060 g KBr and subjected to ultra-sonication for 10 minutes. The mixture was shaken properly at room temperature for a proper time before being moved to a 20 mL Teflon-lined stainless steel autoclave. It was then heated at 120°C for a duration of 10 hours. When the reaction was complete, the autoclave was left to cool down on its own. As a result of this we get white precipitate at the bottom of autoclave. Then we centrifuge it at 8000rpm for 8 minutes, and washed several times with de-ionized water and ethanol. After this we dried it in oven in which atmosphere is without air at 60°C for overnight. As a result of this we obtained white powder.



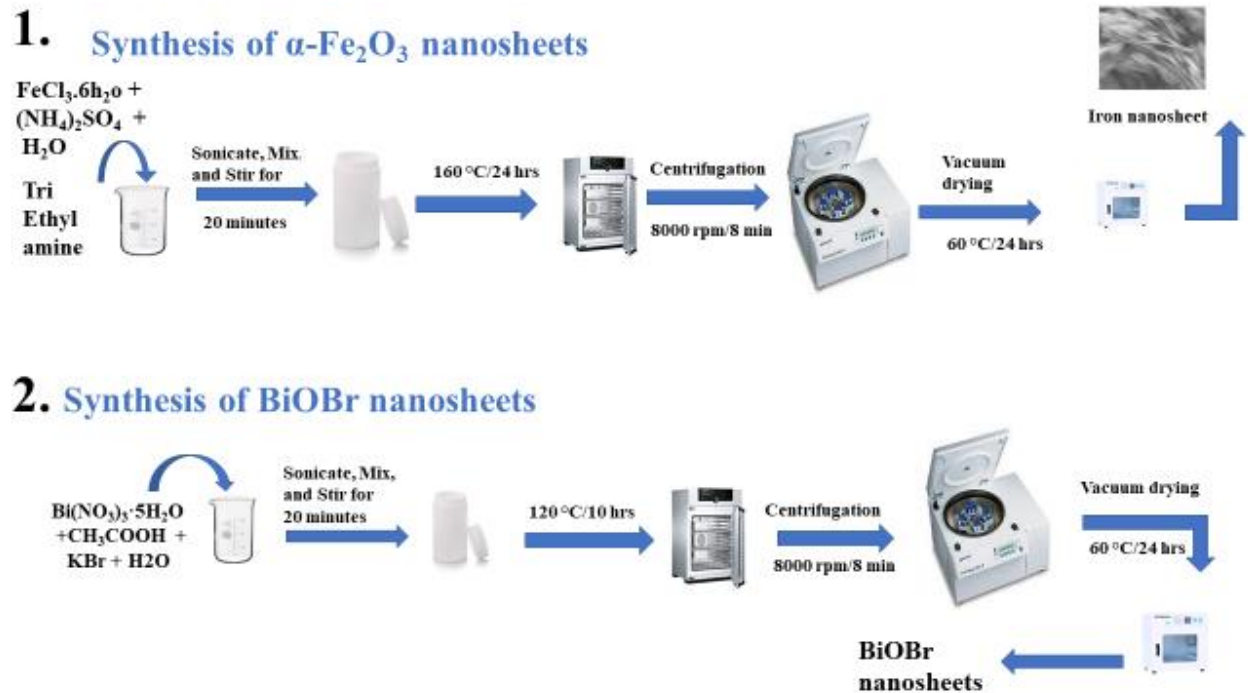


**Figure 12:** Synthesis of  $\alpha$ -Fe<sub>2</sub>O<sub>3</sub> and BiOBr

### 3.5 Synthesis of MoS<sub>2</sub>

MoS<sub>2</sub> nanostructures were created in the experiments using a straightforward hydrothermal technique. None of the chemical reagents that were bought and used needed to be further purified; they were all of analytical quality. In the experiment, 100 mL beakers were filled with a mixture of 1.6 g of Na<sub>2</sub>MoO<sub>4</sub>·2H<sub>2</sub>O and 0.435 g S. Each mixture was then given 12 mL of 85% hydrazine monohydrate (N<sub>2</sub>H<sub>4</sub>H<sub>2</sub>O) as a reducing agent and 20 mL of distilled water. The mixtures were continuously stirred for 30 minutes before being put into a 50 mL Teflon-lined stainless steel autoclave. The autoclave was filled with additional distilled water until it was 80% full. The autoclaves were well-sealed and kept at 180°C for 40 hours in an air oven. The final reaction products were centrifuged after being repeatedly rinsed with distilled water, diluted hydrochloric

acid (HCl), and ethanol after being brought to room temperature. The resulting black precipitates were gathered and dried for 30 hours at 60°C in a vacuum.

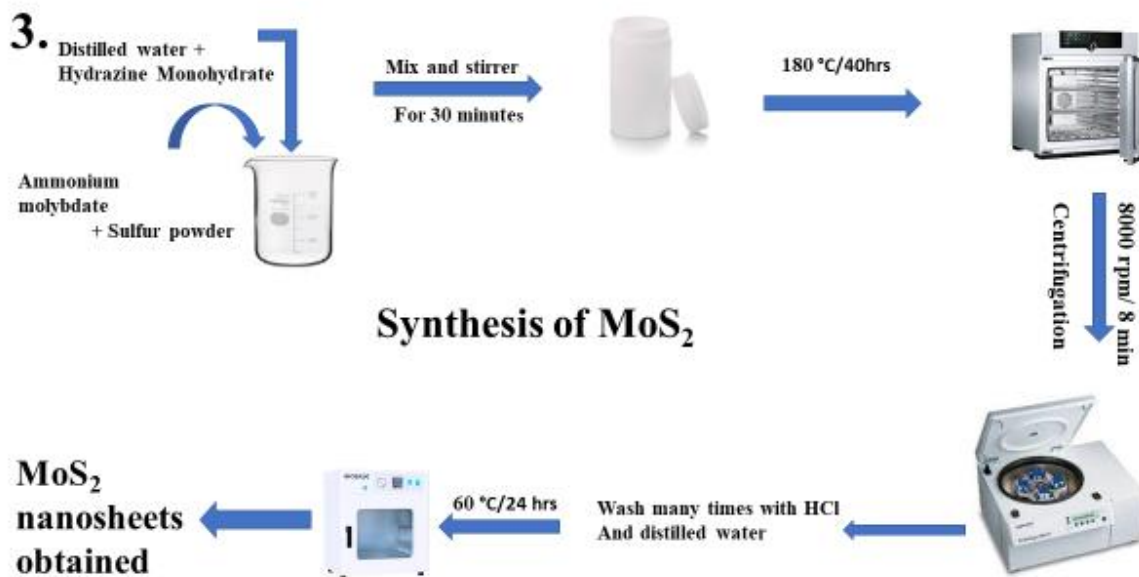


**Figure 13:** Synthesis of MoS<sub>2</sub>

To confirm their composition and crystalline structure, all of these products were examined using various analytical techniques, such as X-ray diffraction (XRD), scanning electron microscopy (SEM), and energy dispersive X-ray spectroscopy (EDS).

### **3.6 Establishment of $\alpha$ -Fe<sub>2</sub>O<sub>3</sub> / BiOBr**

The Fe<sub>2</sub>O<sub>3</sub>/BiOBr composite can be created using a simple and efficient process. In the beginning, an autoclave lined with Teflon is used to prepare a precursor solution of Fe<sub>2</sub>O<sub>3</sub>. To create the composite material, a precise amount of BiOBr is added to the precursor solution in predefined percentages (such as 0.5%, 1%, 5%, 10%, 15%, 20%, or 30%). A extremely favourable nanoscale heterojunction interface between BiOBr and Fe<sub>2</sub>O<sub>3</sub> is made possible by the inclusion of BiOBr. Compared to either individual material, the attributes of this heterojunction are improved. The creation of Fe<sub>2</sub>O<sub>3</sub> / BiOBr composite materials and its use in energy storage and conversion, water splitting, and environmental cleanup have been extensively covered in a number of publications. These investigations have shown that adding BiOBr to Fe<sub>2</sub>O<sub>3</sub> improves the composite material's photoconversion efficiency, stability, and resistance to deterioration. The synthesis conditions, the BiOBr to Fe<sub>2</sub>O<sub>3</sub> ratio, and the composite structure must all be taken into account in order to further improve and optimise the synthesis of the BiOBr/Fe<sub>2</sub>O<sub>3</sub> composite. These variables can be adjusted and optimised to create high-performance g-BiOBr/Fe<sub>2</sub>O<sub>3</sub> composite materials that are suited for certain applications.

### **3.7 Establishment of $\alpha$ -Fe<sub>2</sub>O<sub>3</sub>/BiOBr/MoS<sub>2</sub>**

The Fe<sub>2</sub>O<sub>3</sub>/BiOBr/MoS<sub>2</sub> ternary composite can be created using a simple and efficient process. In the beginning, an autoclave lined with Teflon is used to prepare a precursor solution of Fe<sub>2</sub>O<sub>3</sub> and precise amount of BiOBr and form a binary composite with described conditions. To

create the ternary composite material, a precise amount of  $\text{MoS}_2$  is added to the precursor solution in predefined percentages (such as 5%, 10%, 20%) and form ternary composite. A extremely favourable nanoscale heterojunction interface between  $\text{BiOBr}/\text{Fe}_2\text{O}_3$  is made possible by the inclusion of  $\text{MoS}_2$ . Compared to either binary material, the attributes of this heterojunction are improved. The creation of  $\text{Fe}_2\text{O}_3/\text{BiOBr}/\text{MoS}_2$  ternary composite materials and its use in energy storage and conversion, water splitting, and environmental cleanup have been extensively covered in a number of publications. These investigations have shown that adding  $\text{MoS}_2$  to  $\text{BiOBr}/\text{Fe}_2\text{O}_3$  improves the composite material's photoconversion efficiency, stability, and resistance to deterioration. The synthesis conditions, the  $\text{MoS}_2$  to  $\text{BiOBr}/\text{Fe}_2\text{O}_3$  ratio, and the composite structure must all be taken into account in order to further improve and optimise the synthesis of the  $\text{MoS}_2/\text{BiOBr}/\text{Fe}_2\text{O}_3$  composite. These variables can be adjusted and optimised to create high-performance  $\text{MoS}_2/\text{BiOBr}/\text{Fe}_2\text{O}_3$  composite materials that are suited for certain applications.

## Chapter 4: Characterizations

### 4.1 X-ray diffraction (XRD)

A specific characterization used in materials research to determine a material's crystallographic structure is X-ray diffraction analysis (XRD). XRD first bombards a material with incident X-rays in order to quantify the intensities and scattering angles of the X-rays that leave it.

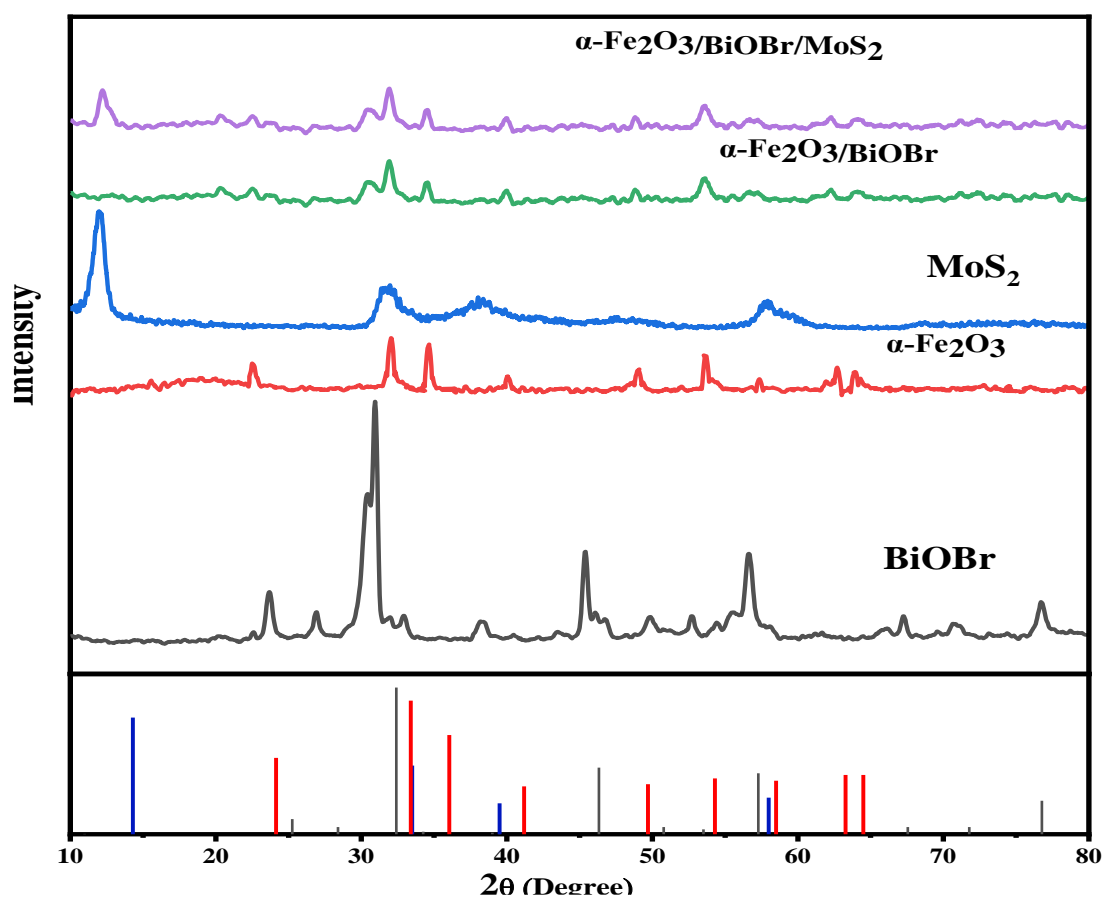


**Figure 14:** XRD pattern of  $\alpha\text{-Fe}_2\text{O}_3$ ,  $\text{BiOBr}$ ,  $\text{MoS}_2$ ,  $\alpha\text{-Fe}_2\text{O}_3 / \text{BiOBr}$  and  $\alpha\text{-Fe}_2\text{O}_3 / \text{BiOBr} / \text{MoS}_2$

X-ray diffraction (XRD) patterns were studied to gain additional insight into the phase and crystalline structure of  $\text{BiOBr}$ . The tetragonal structure (JCPDS No. 09-0393) and the XRD pattern of  $\text{BiOBr}$  in figure were very similar. It also proves that there are no impurity peaks in the XRD

pattern. The XRD pattern reveals that the diffraction peaks of the BiOBr catalyst were discovered at  $2\theta = 10.75^\circ, 25.3^\circ, 28.4^\circ, 31.87^\circ, 32.45^\circ, 34.27^\circ, 46.49^\circ, 50.78^\circ, 53.17^\circ, 57.34^\circ, 67.48^\circ,$  and  $76.79^\circ$  crystal planes of the tetragonal wurtzite structure of BiOBr, respectively. These planes correspond to the reflection from (001,) (002), (102), (110), (111), (112), (200), (014), (211), (212), (220), and (311) planes, respectively.

$\text{Fe}_2\text{O}_3$  sample's XRD pattern after 24 hours at  $160^\circ\text{C}$ . All of the diffraction peaks might, in theory, be quickly identified as pure rhombohedral  $\text{-Fe}_2\text{O}_3$  (JCPDS file Card, no. 33-0664). As the reaction period was extended, the peaks of the XRD diffraction patterns for  $\text{-Fe}_2\text{O}_3$  were narrower. These narrower peaks indicated that the  $\text{-Fe}_2\text{O}_3$  samples were more highly crystalline, and they proved that this process could produce iron oxide nanocrystallines. No additional peaks were seen, demonstrating the great purity of the samples after preparation. The XRD pattern reveals that the diffraction peaks of the  $\alpha\text{-Fe}_2\text{O}_3$  catalyst were discovered at  $2\theta = 24.71^\circ, 33.64^\circ, 35.90^\circ, 41.27^\circ, 44.99^\circ, 54.53^\circ, 63.18^\circ, 64.47^\circ, 72.78^\circ, 75.63^\circ$  and  $78.78^\circ$  crystal planes of rhombohedral  $\alpha\text{-Fe}_2\text{O}_3$ . These planes correspond to the reflection from (012), (104), (110), (113), (024), (116), (214), (300), and (311) planes, respectively.

## 4.2 Scanning electron microscopy (SEM)

Both BiOBr and  $\text{Fe}_2\text{O}_3$  are semiconducting materials with unique morphologies. Scanning electron microscopy (SEM) was used to analyze the shapes and morphological composition of the samples. BiOBr showed a significant large-scale sheet-like structure. The great purity of the synthesized product was particularly evident from the SEM pictures, which showed no detectable imperfections.

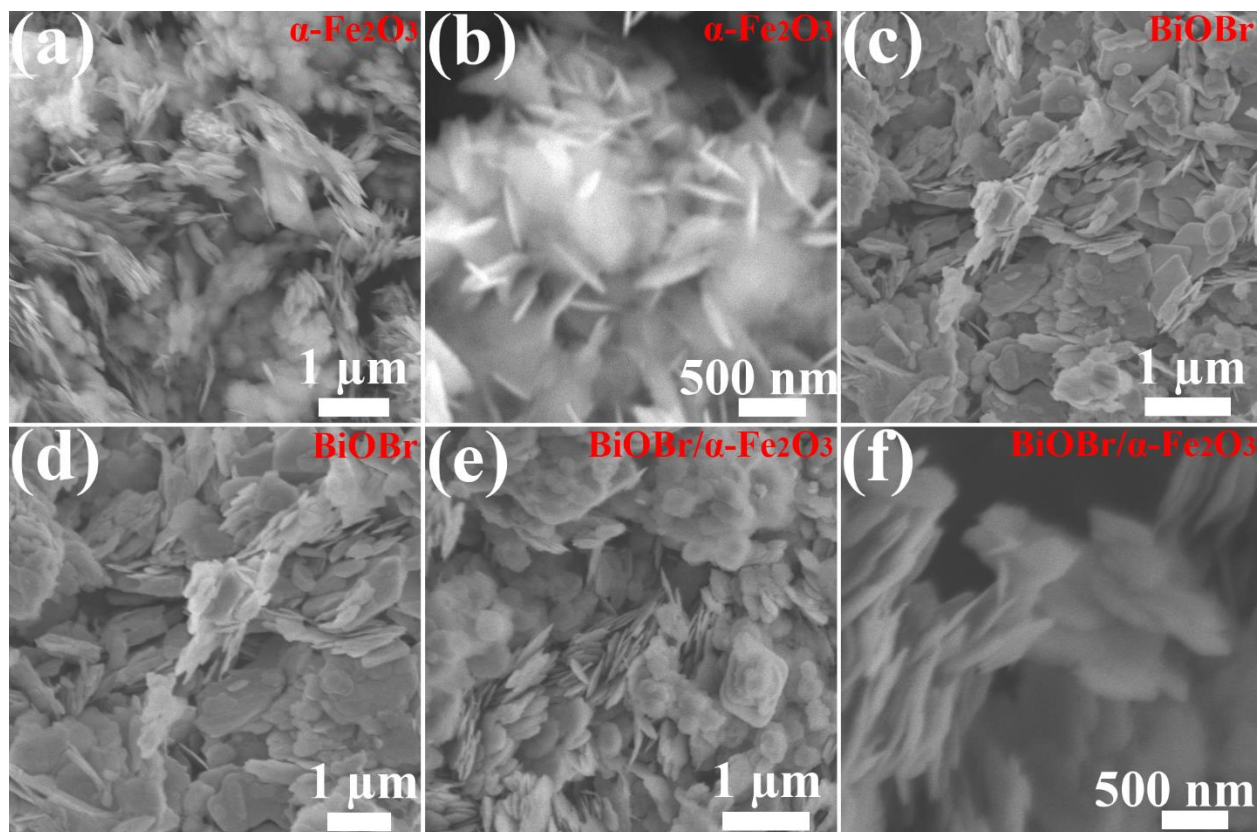


**Figure 15:** (a, b) ultrathin nanosheets of  $\text{Fe}_2\text{O}_3$ , (c, d) nanosheets of BiOBr and (e, f) are SEM images of binary ( $\alpha\text{-Fe}_2\text{O}_3$  / BiOBr) composites.

The tetragonal crystal structure of BiOBr, which promotes the production of thin, malleable sheets along particular crystallographic planes, is responsible for this behavior. These results

support the X-ray diffraction (XRD) analysis' findings and further attest to the reliability and excellence of the nanosheets. However, SEM analysis reveals that pure  $\text{Fe}_2\text{O}_3$  is made up of 2D nanosheets. The resultant product's flexible and ultrathin sheet-like structure is clearly seen in a TEM image. The increased surface tension causes the nanosheets edges to roll up similarly to graphene. After all pristine we see the SEM of binary composite we can easily see the nanosheets of bismuth with the ultra-thin nanosheets of iron oxide, which clearly tells us the binary composite is a 2D material. And by the SEM images of binary composite we can clarify that our binary heterojunction is successfully formed and best for efficient working. All these confirmation can also be present in the SEM images of the ternary composites. Which is successful in their working and perform good results in water splitting.

Shape can affect the physical and chemical properties of all of these materials, including surface area, electronic structure, and catalytic activity. Understanding these materials' morphology is essential for designing and maximizing their applications in a range of fields, including photocatalysis and energy conversion.



### 4.3 HR-TEM

Transmission electron microscopy (TEM) and high-resolution TEM (HRTEM) are powerful tools for characterizing the morphology and crystal structure of materials at the nanoscale. In the instance of  $\alpha$ -Fe<sub>2</sub>O<sub>3</sub>, BiOBr and MoS<sub>2</sub> composites, TEM examination has shown that the synthesised  $\alpha$ -Fe<sub>2</sub>O<sub>3</sub> contains 2D uniform ultrathin nanosheets (NSs) with a curling shape that are almost transparent and flexible. The hexagonal crystal structure of  $\alpha$ -Fe<sub>2</sub>O<sub>3</sub>, which causes the creation of thin and flexible sheets along specific crystallographic planes, is related to the great flexibility and thinness of these sheets. The  $\alpha$ -Fe<sub>2</sub>O<sub>3</sub> sheets are adorned with BiOBr and MoS<sub>2</sub> sheets, generating nanoheterojunctions, as further evidenced by the TEM and HRTEM images.

The BiOBr can be somewhat prevented from aggregating by being immobilised by anchor sites provided by the 2D  $\alpha$ -Fe<sub>2</sub>O<sub>3</sub> nanosheets. As a result, the specific surface area of the composites rises in comparison to pure  $\alpha$ -Fe<sub>2</sub>O<sub>3</sub>. In the area of photocatalysis and energy conversion, the development of such nanoheterojunctions is quite interesting since it can improve the performance of these materials by encouraging charge separation and transfer. Designing and maximising these composites' uses in a variety of disciplines consequently requires an understanding of their shape and crystal structure.

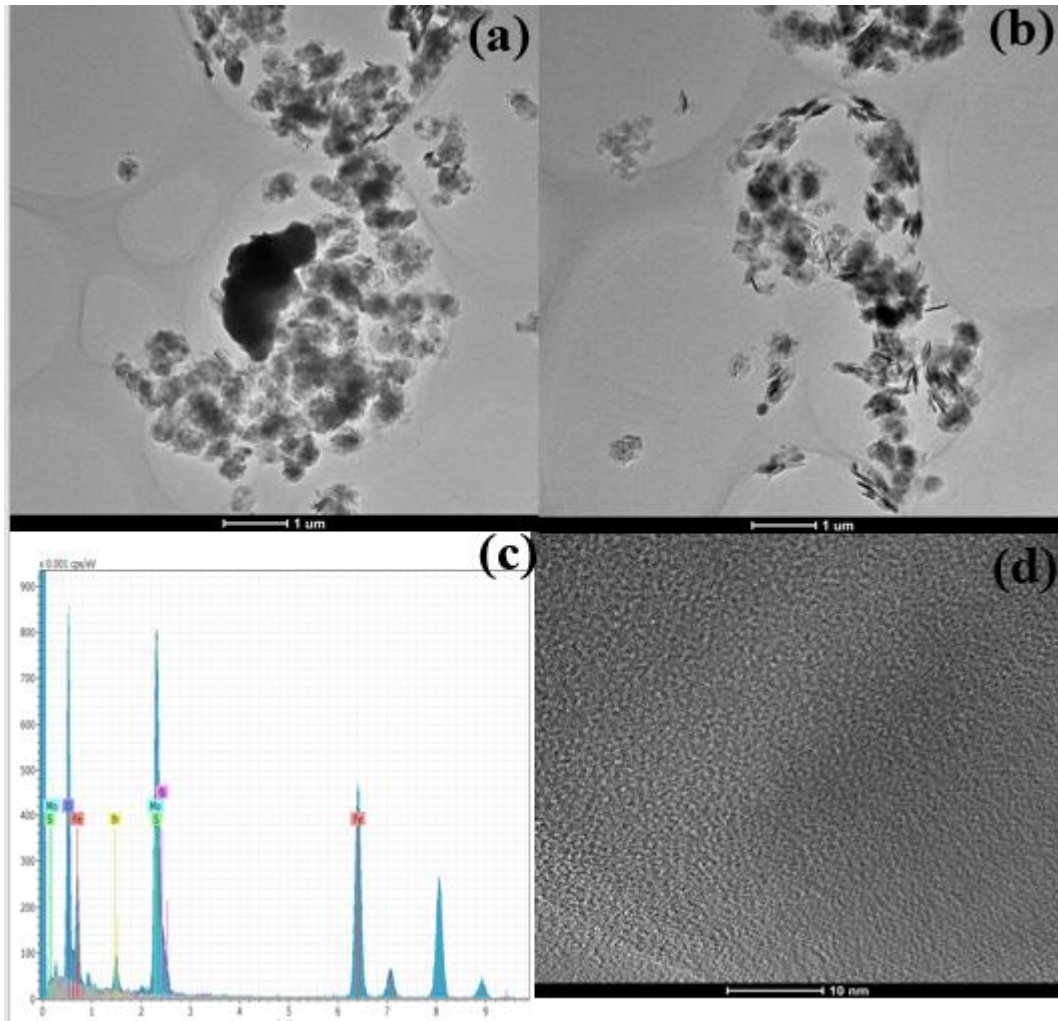


**Figure 16:** (a, b) HR-TEM images of  $\alpha\text{-Fe}_2\text{O}_3/\text{BiOBr}/\text{MoS}_2$  (c) EDS-spectra of  $\alpha\text{-Fe}_2\text{O}_3/\text{BiOBr}/\text{MoS}_2$

EDS, which is also named as energy-dispersive X-ray spectroscopy, is a methodology for determining the elemental makeup of materials at the nanoscale.  $\text{MoS}_2/\text{BiOBr}/\text{Fe}_2\text{O}_3$  nano heterojunctions are an example. Following TEM imaging, EDS analysis verifies the presence of each element in the composite.

The presence of cadmium in the composite is shown by the EDS spectrum's Fe and O peak appearances shows the presence of  $\alpha\text{-Fe}_2\text{O}_3$ . The presence of sulphur and molbydenum is shown

by the peak for S and Mo, as would be predicted for MoS<sub>2</sub>. Peaks of Bi, Br and O further demonstrate the presence of BiOBr in the composite. Understanding the composite's constituent makeup is crucial for comprehending both its physical and chemical characteristics. The coexistence of both substances in  $\alpha$ -Fe<sub>2</sub>O<sub>3</sub>/BiOBr/MoS<sub>2</sub> nanoheterojunctions produces a synergistic effect that can improve their photocatalytic activity. Understanding the two materials' presence in the composite through the EDS analysis is essential for comprehending its characteristics and behaviour.

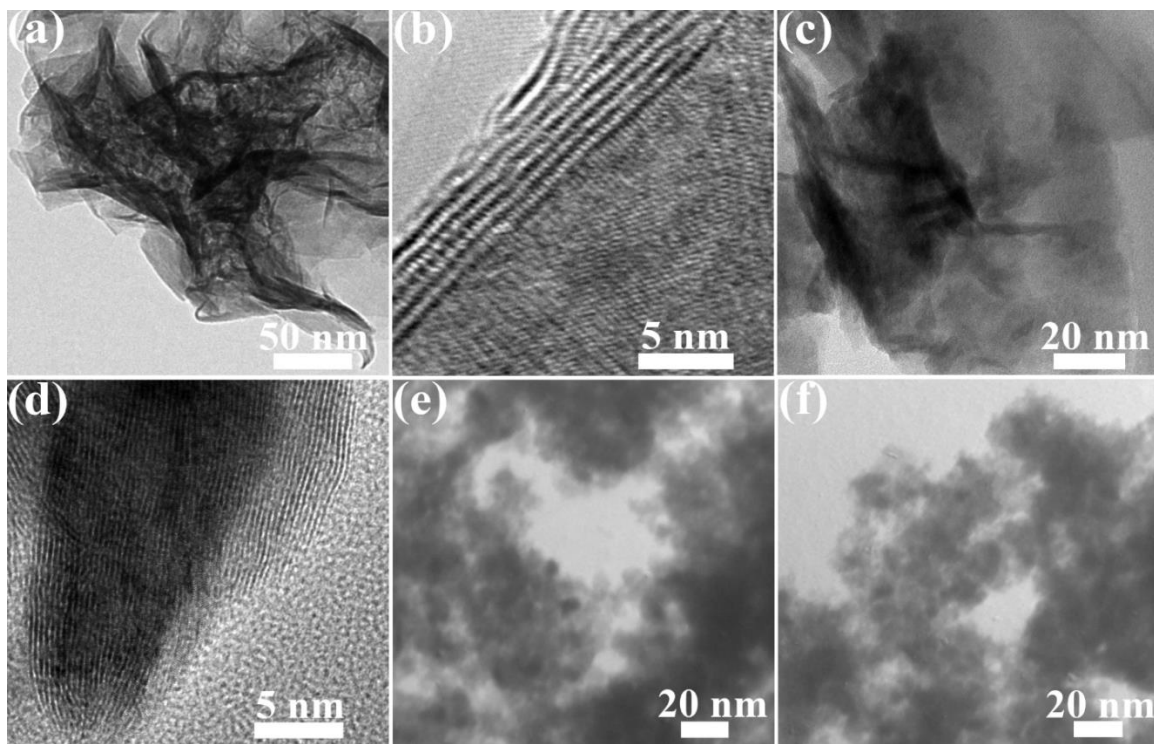


**Figure: 17** HR-TEM analysis of (a, b) few-layer nanosheets of MoS<sub>2</sub>, (c, d) Multi-layered nanosheets of MoS<sub>2</sub>, (e, f) MoS<sub>2</sub> nanoparticles.

In image (a, b) we can clearly see that the thin and completely exfoliated few layered MoS<sub>2</sub> nanosheets which are Nearly transparent and Thin nanosheets and provide more area for the reaction and are best in morphology. In the image (c, d) there are multi-layered nanosheets of MoS<sub>2</sub>, which are present in bulk amounts and not completely exfoliated and comparatively less suitable for reaction. In the image (e, f) there are nanoparticles of MoS<sub>2</sub>. The TEM and HRTEM images further reveal that the MoS<sub>2</sub> are provides less sites for the composition of nanoheterojunction.

#### **4.4 Elemental Mapping**

A method for displaying the spatial distribution of elements in a substance is called elemental mapping. The elemental mapping of the MoS<sub>2</sub> /BiOBr/ Fe<sub>2</sub>O<sub>3</sub> composite reveals that the elements *bismuth* (Bi), bromine (Br), Iron (Fe) carbon (C), Molybdenum (Mo), Sulphur(S) and Oxygen (O) are distributed uniformly throughout the 2D sheet-like structure. Knowing this information is crucial for comprehending the make-up and structure of the composite. The Fe<sub>2</sub>O<sub>3</sub>, BiOBr, and MoS<sub>2</sub> components are likely to be present because of the elements' consistent distribution. These are evenly and thoroughly distributed throughout the composite. It is desirable to accomplish this. A uniform distribution of the active ingredients can prevent the photocatalytic system from operating at its best to increase energy transfer and charge separation efficiency.

In general, elemental mapping is a useful method for describing the structure and composition of materials at the nanoscale. Researchers can learn more about the behavior and efficiency of materials in a variety of applications, such as photocatalysis and energy conversion, by visualizing the distribution of the elements.

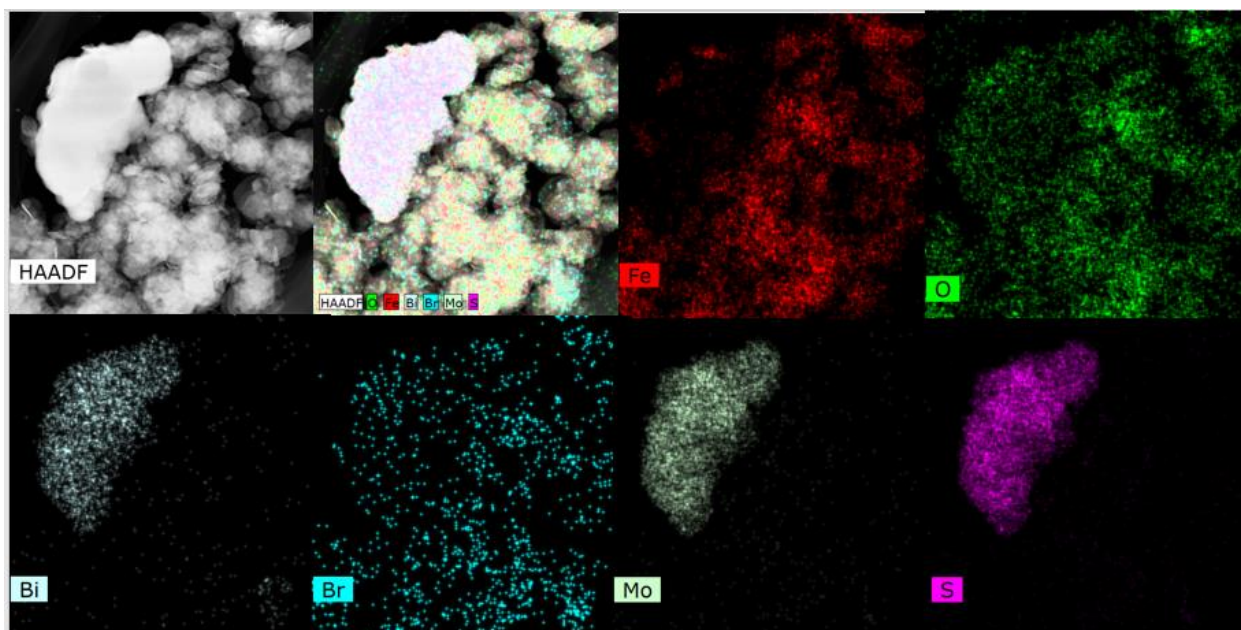


**Figure 18:** Elemental mapping of  $\text{MoS}_2/\text{BiOBr}/\text{Fe}_2\text{O}_3$

#### 4.5 X-ray photoelectron spectroscopy (XPS)

By analyzing the materials using X-ray photoelectron spectroscopy (XPS), the chemical composition of the substances was determined. An effective method for determining the chemical makeup and element valence of the  $\text{Fe}_2\text{O}_3/\text{BiOBr}/\text{MoS}_2$  composite is the X-ray photoelectron spectroscopy (XPS) examination. The typical XPS survey spectrum (Fig. a) reveals the presence of the elements Bi, O, Br, Mo, Fe, S, and C, proving once again that the ternary  $\text{Fe}_2\text{O}_3/\text{BiOBr}/\text{MoS}_2$  composite is composed of Bi, O, Br, Mo, S and Fe elements. In figure (b) The presence of  $\text{Fe}^{3+}$  and  $\text{Fe}^{2+}$  in the sample is confirmed by the Fe 2p binding energies of 711.3 and 729.0 eV, which are attributed to Fe 2p<sub>3/2</sub> and Fe 2p<sub>1/2</sub>, respectively. In Figure (c) The adventitious carbon serves as the reference for the binding energies of other elements, with C1s at 284.6 eV and 288.8 eV.

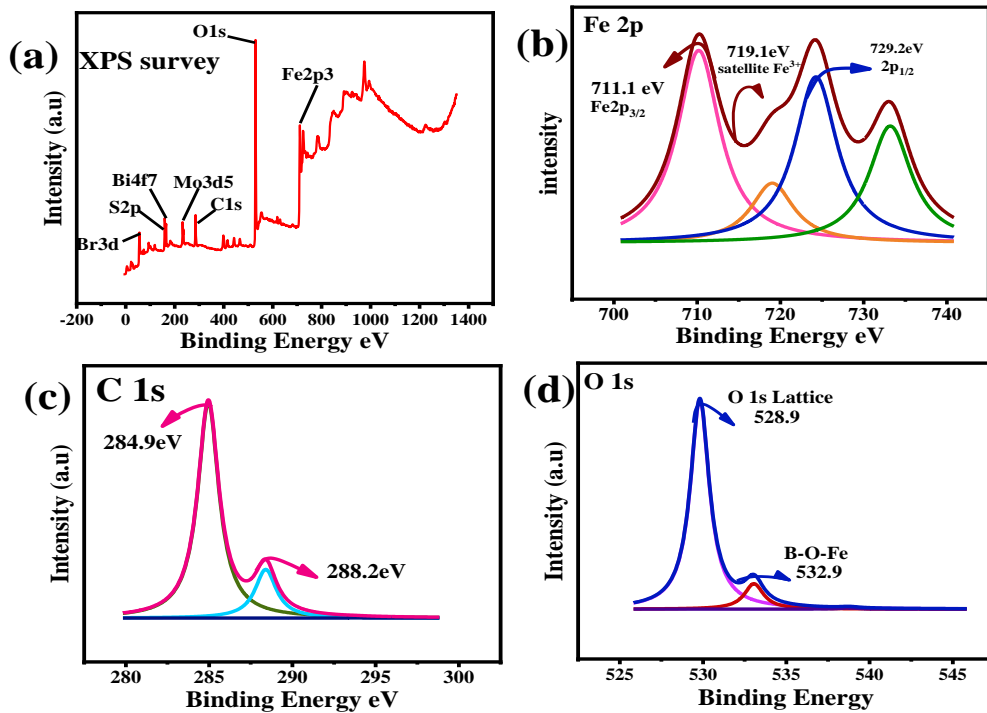


**Figure 19:** XPS spectrum of Fe 2p, C 1S, and O 1S

In Figure (d) Regarding the O 1s, there are two distinct oxygen species visible: the strong peak at 528.2 eV is due to the lattice oxygen in  $\text{Fe}_2\text{O}_3/\text{BiOBr}/\text{MoS}_2$ , and the binding energy at 532.5 eV is a result of the hydroxyl groups connected to the surface of the magnetic catalyst. In Figure (e) the peaks for Bi 4f are noticed from the spectra, and they contain peaks for Bi  $4f_{7/2}$  (Bi (III)) at 159.1 eV and Bi  $4f_{5/2}$  (Bi (V)) at 165.1 eV. In Figure (f) Br  $3d_{5/2}$  and Br  $3d_{3/2}$  peaks, which have binding energies of 68.8 and 75.2 eV, respectively. The Mo3d spectra in Figure (g) has two clear peaks at 228.8 eV ( $\text{Mo}3d_{5/2}$ ) and 232.0 eV ( $\text{Mo}3d_{3/2}$ ), as well as a little signal at 226.1 eV that is attributed to S2s. The Mo(VI) oxidation state is also attributed to the  $\text{Mo}3d_{5/2}$  and  $\text{Mo}3d_{3/2}$  peaks at 235.7 eV, 232.7 eV, and 229.4 eV, respectively.

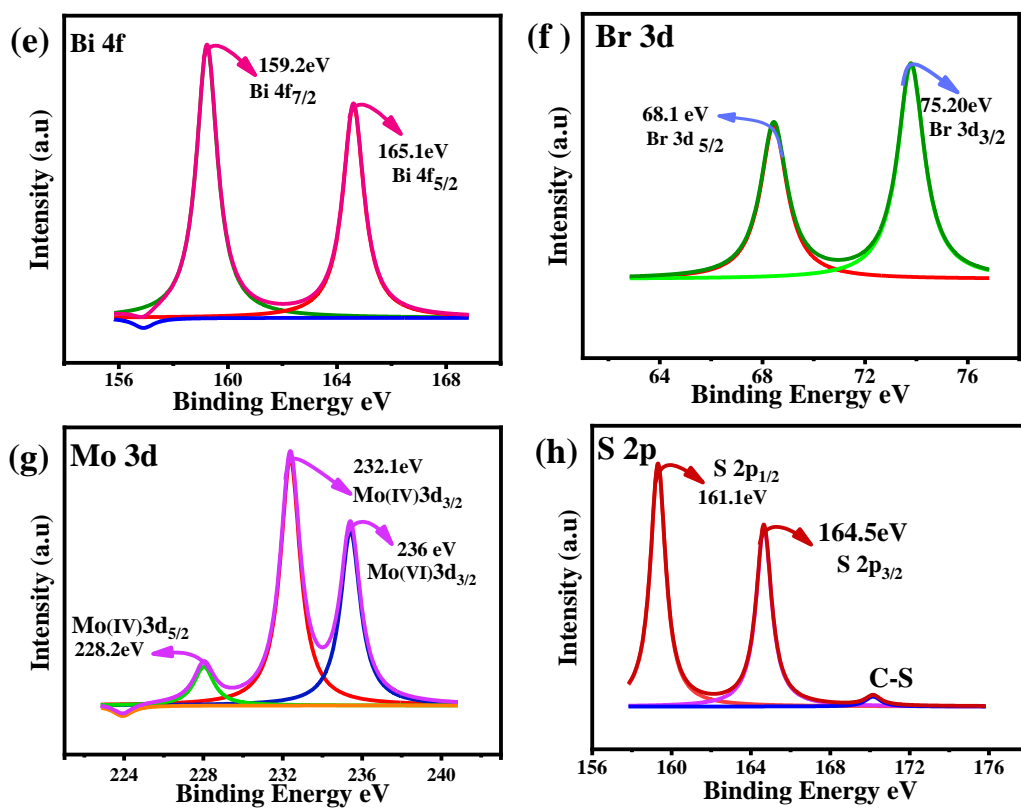


**Figure 20:** XPS spectrum of BI 4f, Br 3d, Mo 3d, and S 2p.

In Figure (h) there are two significant peaks at 164.0 eV and 161.7 eV, corresponding to the  $S_{2p_{1/2}}$  and  $S_{2p_{3/2}}$  binding energies for  $S^{2-}$ , which are visible in the  $S_{2p}$  spectra. And the presence of sulfate groups could be the cause of the peak at 169.2 eV.  $Fe_2O_3$ ,  $BiOBr$ , and  $MoS_2$  are found to coexist in the ternary magnetic composite  $\alpha\text{-}Fe_2O_3 / BiOBr / MoS_2$  using XPS analysis, which is consistent with the findings of XRD and SEM examination.

#### 4.6 Diffuse reflectance spectroscopy (DRS)

Diffuse reflectance spectroscopy (DRS) is a method for examining a material's electrical characteristics. DRS analysis can be used to determine the band gap of the  $\alpha\text{-}Fe_2O_3$ ,  $BiOBr$  and

MoS<sub>2</sub> composite material. The Tauc plot is used to extrapolate the curve generated by plotting  $(F(R)hv)^2$  versus Energy, and the Kubelka-Munk transformation is used to convert the fraction of reflected light into absorbance. This makes it possible to calculate the composite material's band gap. The calculated band gap values for the  $\alpha$ -Fe<sub>2</sub>O<sub>3</sub>, BiOBr, MoS<sub>2</sub>,  $\alpha$ -Fe<sub>2</sub>O<sub>3</sub>/BiOBr and  $\alpha$ -Fe<sub>2</sub>O<sub>3</sub>/BiOBr/ MoS<sub>2</sub> S-Scheme heterojunction composite, respectively, are 2 eV, 2.67 eV, 1.7, eV, 2 eV and 1.8 eV which point to a reduction in band gap and the establishment of heterojunction.

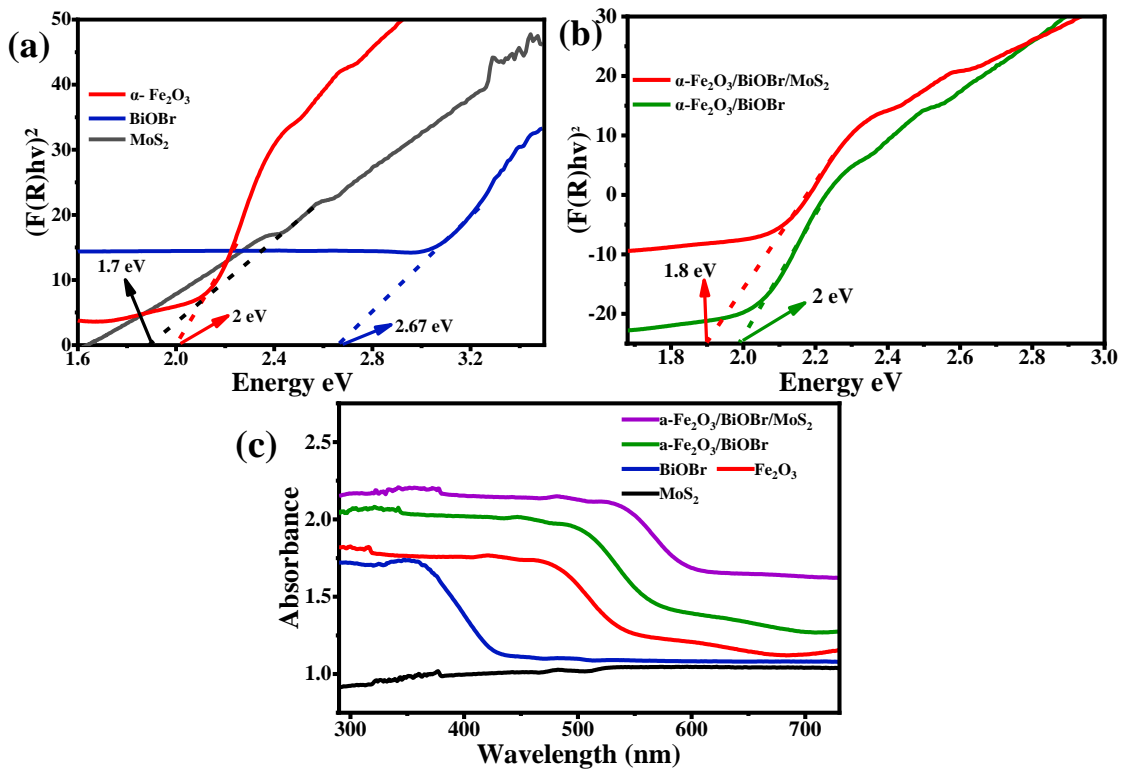


**Figure 21:** DRS Analysis of  $\alpha$ -Fe<sub>2</sub>O<sub>3</sub>, BiOBr, MoS<sub>2</sub>,  $\alpha$ -Fe<sub>2</sub>O<sub>3</sub>/BiOBr and  $\alpha$ -Fe<sub>2</sub>O<sub>3</sub>/BiOBr/ MoS<sub>2</sub>

This reduction in band gap suggests that the composite material will be better able to use visible light, which is advantageous for prospective uses in photocatalysis or solar cells. The



technique employed for the investigation has a solid foundation in the academic literature and is frequently applied to find band gaps in a variety of materials.

#### 4.7 Photoluminescence Spectroscopy (PL Analysis)

A molecule absorbs a light energy in the visible spectrum that excite one of its electrons to a higher electrical excited state and then emits a photon as the electron returns to a lower energy state. This process is known as photoluminescence.

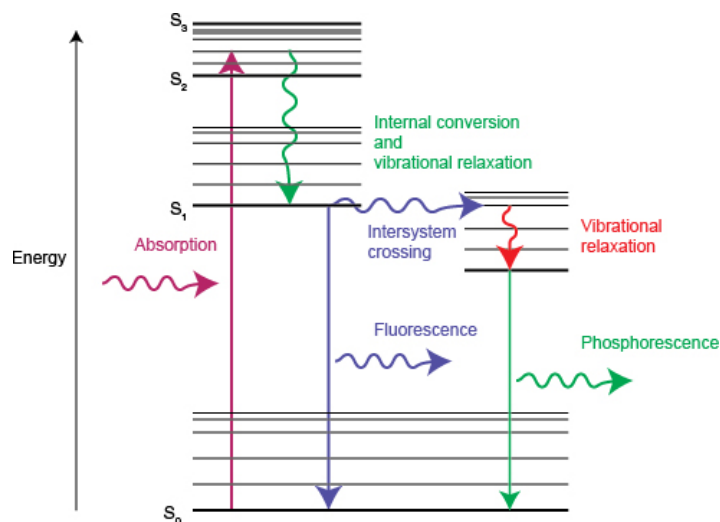


**Figure 22:** Energy diagram displaying the processes involved in emitting light, such as fluorescence and phosphorescence, as well as how light is absorbed.

Fluorescence and phosphorescence processes interact with one another during absorption and emission to produce PL, which is made up of both of these processes. Depending on the substance being researched and the laser wavelength being employed, different types and amounts of PL are produced. By choosing the proper laser wavelength, undesired fluorescence interference can typically be avoided.

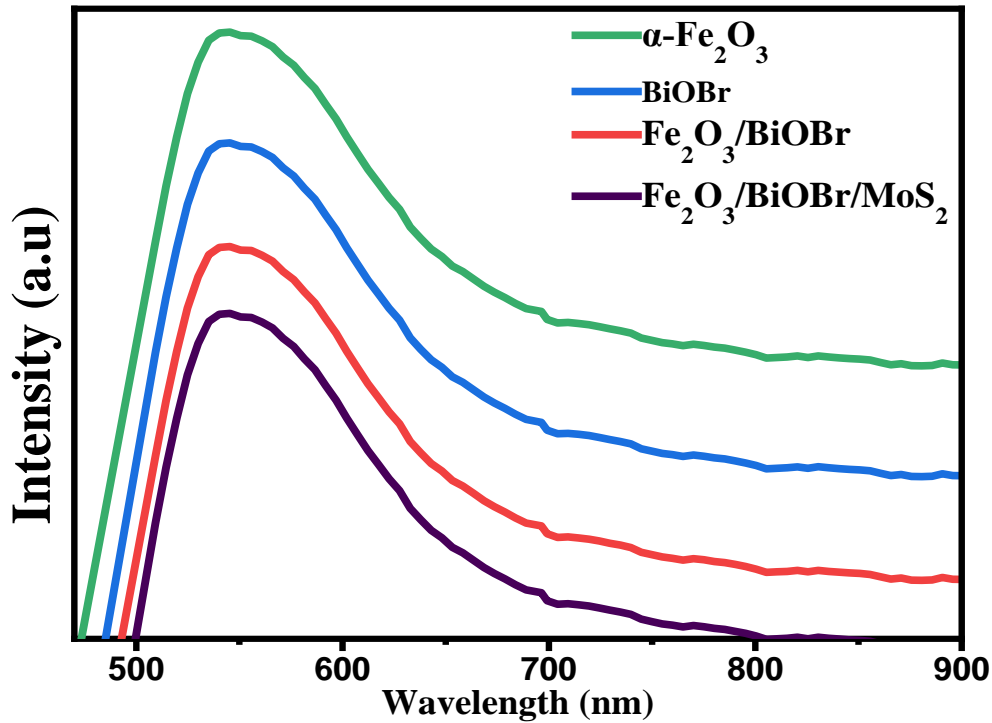


**Figure 23:** PL of  $\text{Fe}_2\text{O}_3$ , BiOBr and binary ( $\alpha\text{-Fe}_2\text{O}_3$  / BiOBr) composites.

In this example, the charge transport and separation efficiency of  $\alpha\text{-Fe}_2\text{O}_3/\text{BiOBr}/\text{MoS}_2$  heterojunctions were studied using the potent technique of photoluminescence spectroscopy (PL), which is utilized to investigate the electronic properties of materials. A 414 nm excitation wavelength was used in the PL analysis to examine the material's light emission. Information on the charge recombination process in the material is revealed by the intensity of the PL spectra. According to the findings, BiOBr has a substantially lower intensity peak than  $\alpha\text{-Fe}_2\text{O}_3$  which has the largest intensity peak and the highest charge recombination rate. The  $\alpha\text{-Fe}_2\text{O}_3$  / BiOBr composite exhibits the lowest intensity peak, which shows that there is less charge recombination there than in the original material. The presence of trap centers, flaws at the grain boundaries, band

structure, and carrier mobility in the composite material are just a few of the causes of this decrease in emission intensity. In ternary composite  $\alpha\text{-Fe}_2\text{O}_3/\text{BiOBr}/\text{MoS}_2$  composite exhibits the lowest intensity peak, which shows that there is less charge recombination there than in the original material and binary composite.

All things considered, the PL analysis is a useful technique for understanding the charge transport and separation effectiveness of heterojunctions in composite materials and can help in optimizing the design and functionality of materials for various applications. The analytical methodology is extensively used to study charge recombination processes in a variety of materials and has a proven track record in academic publications.

#### **4.8 Mott-Schotkey**

The Mott-Schottky analysis, one of the most popular electrochemical techniques for determining semiconductor electrical properties, can reveal information about a material's conductivity, band gap, and the specific positions of the valence band (VB) and conduction band (CB). We used the Mott-Schottky curves to show that the BiOBr and pure  $\text{Fe}_2\text{O}_3$ . In this study, both the materials and the composite were n-type. The CB potentials of  $\alpha\text{-Fe}_2\text{O}_3$  and BiOBr were calculated to be -0.85 and -0.36 V vs. NHE using the expected band gap values from the DRS spectra, while the VB positions were determined to be +1.99 and +2.65 V vs. NHE. The negative slope of the Mott-Schottky curves denotes the n-type nature of the materials. The Fermi levels VB

and CB of BiOBr and  $\alpha$ -Fe<sub>2</sub>O<sub>3</sub> simultaneously changed due to electron flow during the composite's production.

When the VB and CB of both components converged to the same value, this equilibrium was reached. The CB of the composite was calculated using the CB of its lowest CB component. The CB potential of  $\alpha$ -Fe<sub>2</sub>O<sub>3</sub>/ BiOBr/MoS<sub>2</sub>, in this case, was + 0.07 V vs. NHE, which is closer to that of MoS<sub>2</sub>, showing that the level of CB MoS<sub>2</sub> was employed to indicate the CB level of the composite. In contrast, the composite's VB was replaced with the VB of  $\alpha$ -Fe<sub>2</sub>O<sub>3</sub>. These results demonstrate that Mott-Schottky analysis can be used to precisely predict the electrical properties of semiconductors and composite materials.

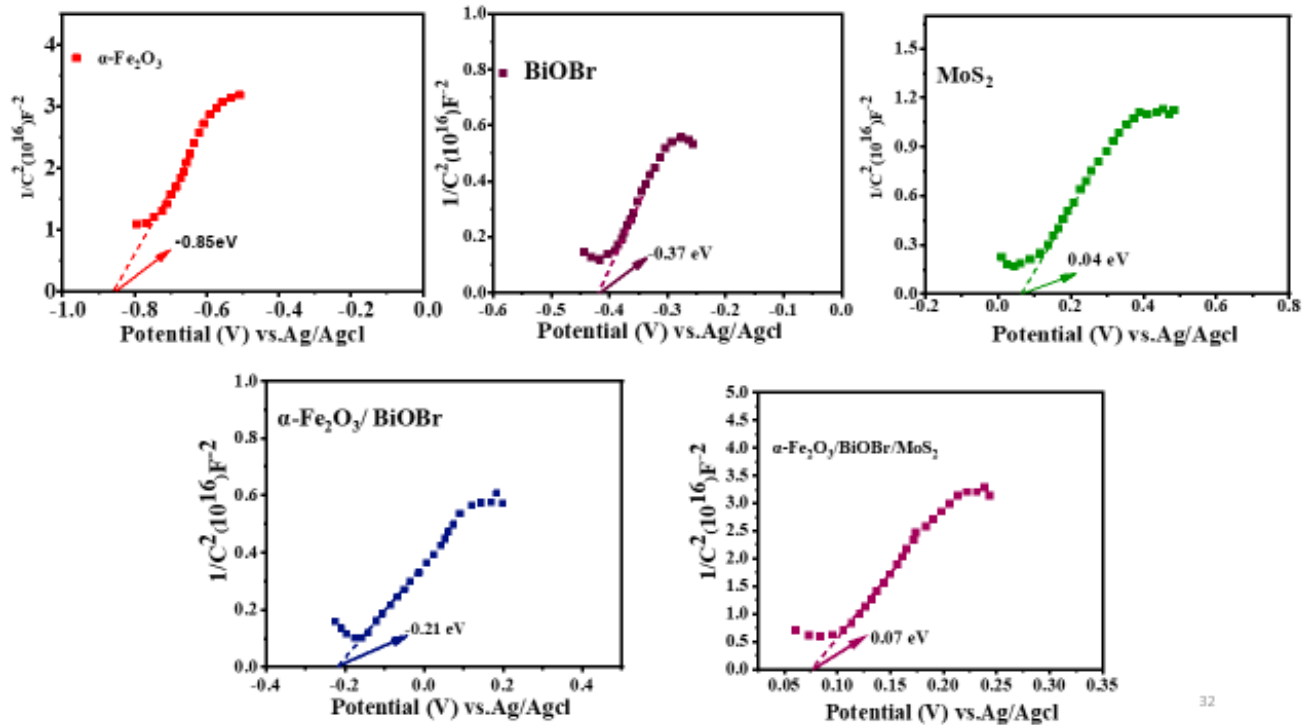


**Figure 23:** Mott-Schotkey Analysis of  $\alpha$ -Fe<sub>2</sub>O<sub>3</sub>, BiOBr, MoS<sub>2</sub>,  $\alpha$ -Fe<sub>2</sub>O<sub>3</sub> / BiOBr and  $\alpha$ -Fe<sub>2</sub>O<sub>3</sub> / BiOBr / MoS<sub>2</sub>

#### 4.9 Chronoamperometric Chopping

A potent method for examining the charge recombination and light response of materials is chronoamperometric chopping (CA). To examine the photocurrent response of the  $\alpha$ -Fe<sub>2</sub>O<sub>3</sub>/BiOBr heterostructure in a 1 M KOH solution under chopping irradiation at 0V, the CA analysis was carried out in the case of  $\alpha$ -Fe<sub>2</sub>O<sub>3</sub> and BiOBr composite. It was decided to chop every 50 seconds at a mild off-on pace. The findings demonstrate that the composite material's photocurrent density of 55  $\mu$ A/cm<sup>2</sup> is much higher than that of the pure materials,  $\alpha$ -Fe<sub>2</sub>O<sub>3</sub> and BiOBr, which were 8  $\mu$ A/cm<sup>2</sup> and 20  $\mu$ A/cm<sup>2</sup>, respectively. The photocurrent density of MoS<sub>2</sub> is 6  $\mu$ A/cm<sup>2</sup> after that. And the current density of ternary composite  $\alpha$ -Fe<sub>2</sub>O<sub>3</sub>/BiOBr/MoS<sub>2</sub> is 70  $\mu$ A/cm<sup>2</sup>. This increase in photocurrent density suggests that the  $\alpha$ -Fe<sub>2</sub>O<sub>3</sub>/BiOBr/MoS<sub>2</sub> heterojunction system's photogenerated charge transport and separation process is extremely effective. Further demonstrating superior charge transport and separation was the composite material's increased current density in the dark. The CA analysis validates the heterojunction system of  $\alpha$ -Fe<sub>2</sub>O<sub>3</sub>/BiOBr/MoS<sub>2</sub>'s ability to facilitate effective charge separation and transport, which is essential for applications in photovoltaic devices and photocatalysis.

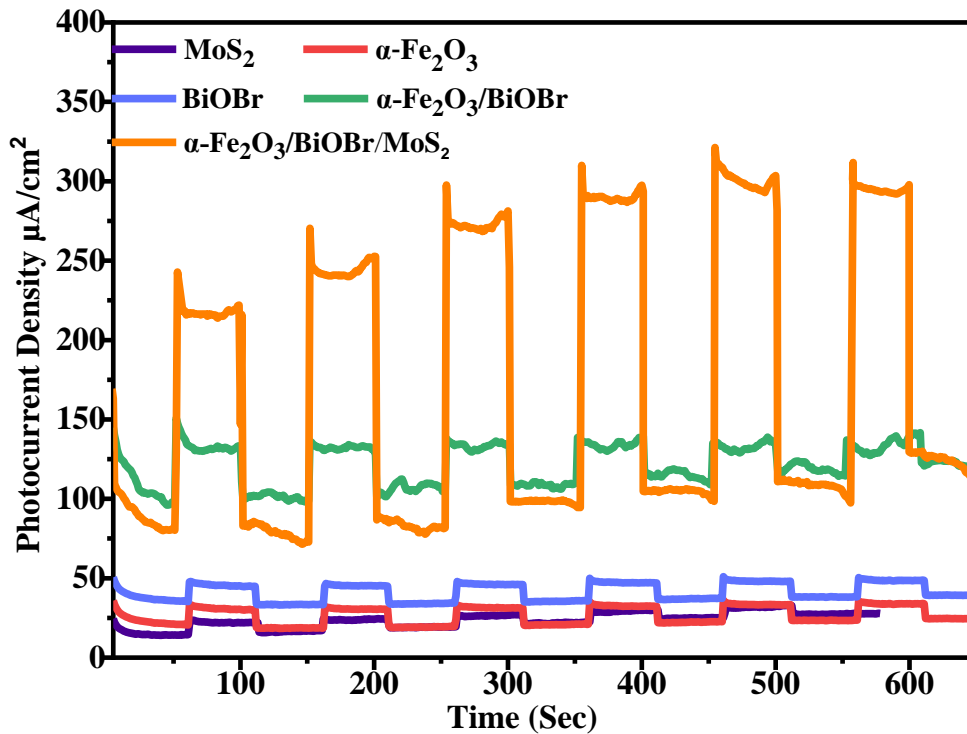


**Figure 24:** Chronoamperometric Chopping of  $\alpha\text{-Fe}_2\text{O}_3$ ,  $\text{BiOBr}$ ,  $\text{MoS}_2$ ,  $\alpha\text{-Fe}_2\text{O}_3/\text{BiOBr}$  and  $\alpha\text{-Fe}_2\text{O}_3/\text{BiOBr}/\text{MoS}_2$

Overall, the CA analysis is a beneficial technique for comprehending charge recombination and light response in materials, and it can aid in improving the design and functionality of materials for a variety of applications. The technique utilized for the analysis has a strong foundation in the scientific literature and is frequently employed to research charge transport and separation processes in a wide range of materials.

#### 4.10 Mechanism Proposal

In order to separate and transport photoinduced negatively electrons and positively holes, which are required for sun light used reactions like the reduction of  $\text{O}_2$  to  $\cdot\text{O}_2$  and the oxidation of  $\text{H}_2\text{O}$  to  $\cdot\text{OH}$ , the heterojunction has an electric field built into it. The electric field is produced

by the flow of electrons from BiOBr to  $\alpha$ -Fe<sub>2</sub>O<sub>3</sub>, which forms an electron-rich zone on the BiOBr side and a reduction layer on the  $\alpha$ -Fe<sub>2</sub>O<sub>3</sub> side. The transport of holes on the VB of  $\alpha$ -Fe<sub>2</sub>O<sub>3</sub> and the transport of electrons on the CB of BiOBr towards the interface may be facilitated by the polarization of the electrical double layer and the buildup of charge carriers at the interface, which may result in a bending up/down of VB maximum and CB minimum. By keeping holes on the VB of BiOBr and electrons on the CB of  $\alpha$ -Fe<sub>2</sub>O<sub>3</sub>, this enables the effective recombination of photoinduced electrons and holes. And there is MoS<sub>2</sub> act as a co-catalyst which take electron from the CB of  $\alpha$ -Fe<sub>2</sub>O<sub>3</sub> and decrease the electron-hole recombination rate. So this is best for the composition of heterojunction and facilitate the reduction of proton and production of hydrogen. Additionally, the recombination of  $\alpha$ -Fe<sub>2</sub>O<sub>3</sub> VB during the release of oxidative holes stabilizing the substance. The  $\alpha$ -Fe<sub>2</sub>O<sub>3</sub>/BiOBr/MoS<sub>2</sub> heterojunction's operation as a photocatalyst is generally explained by this assertion that the heterojunction is S-Scheme.

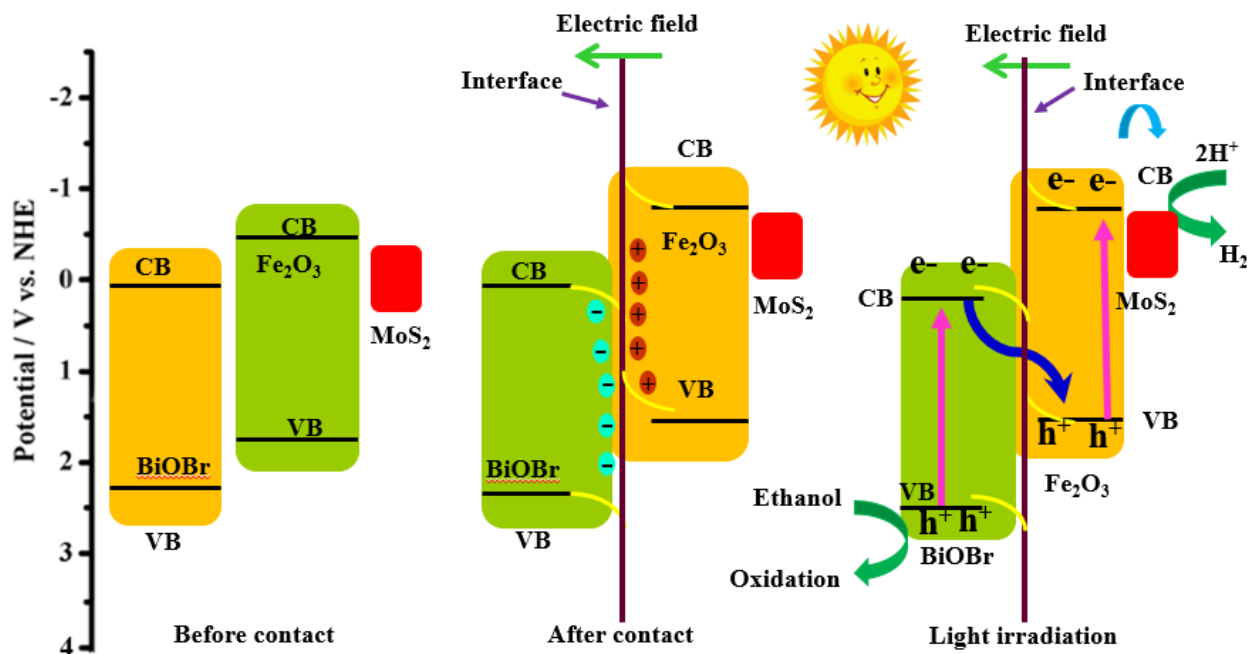


**Figure 25:** S-scheme heterojunction between  $\alpha\text{-Fe}_2\text{O}_3/\text{BiOBr}/\text{MoS}_2$



## Chapter 5: Hydrogen Production (Photocatalytic Activity)

The visible light produced hydrogen production experiments were performed out in a side-irradiation Pyrex cell with magnetic stirring under a 300 W Xe arc lamp and a UV-cut-off filter (420 nm) at room temperature. A 100 ml flask with a flat edge for optimal light irradiation is used for this purpose. First, we take 12 ml of deionized water in a beaker for this, add 0.456 g sodium hydroxide and dissolve it completely, this is for the purpose to maintain the pH upto 13.5. The pH value was adjusted to ensure adequate hole consumption[87]. Then we take 16ml absolute ethanol and fill upto 80ml with mineral water in a 100 ml beaker. And then we add 8-10 mg of our catalyst and after adding catalyst we sonicate it for 20 minutes in an ultra-sonication bath. When it properly sonicate we put sample solution into the one-sided flat flask and degassed it (anaerobic conditions) to make it air free.

Then we close septum properly to avoid removal of gas. Then we put flask in front of lamp near as possible in an appropriate way and cover it properly with the help of aluminum foil. After one an hour we take its first reading with help of 1ml needle, and then we again cover it properly and take second reading after two hours with the help of same volume other needle. Using a detector (TCD), gas chromatography was used to examine the photocatalytic H<sub>2</sub> generation rate. Based on the amount of hydrogen produced during the first hour of the reaction, the average hydrogen formation rates were calculated.

## 5.1 H<sub>2</sub> production by using Ethanol as a sacrificial agent

First of all we check the all pristine material hydrogen production by this mentioned method, our major material is iron oxide which produced hydrogen 2 mmolh<sup>-1</sup>g<sup>-1</sup>. This is very low and undefined amount. After this we move towards heterojunction  $\alpha$ -Fe<sub>2</sub>O<sub>3</sub>/ BiOBr and check its hydrogen production by different ratio. In this way we achieved good results and defined amount of hydrogen production. Here bismuth oxybromide enhanced the ability of iron oxide for hydrogen production, and we get desired results.

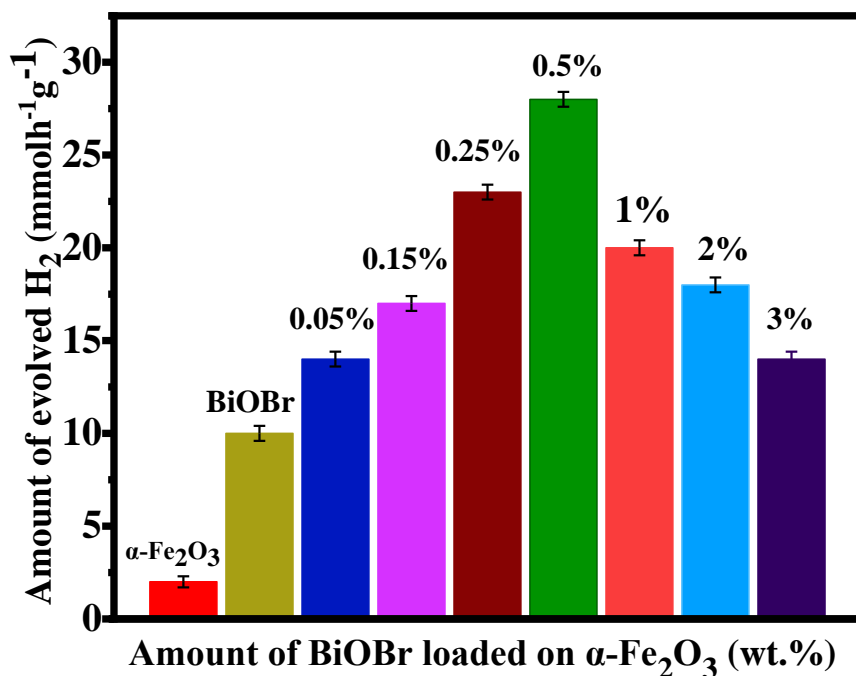


**Figure 26:** H<sub>2</sub> production by using Ethanol as a sacrificial agent by different amount of BiOBr loaded on Fe<sub>2</sub>O<sub>3</sub>

As we know that by combining mixing two or more different metals can improve the catalytic characteristics of transition metal oxides (TMOs). Due to the synergistic coupling effect

between the metal species, bimetallic oxides in particular frequently exhibit stronger HER activity than monometallic oxides while tri-metallic oxides demonstrate significantly more HER activity.

## 5.2 Comparison of Hydrogen production in Binary and Ternary Composites

In this graph we see comparison in binary and ternary composite hydrogen production. After binary composite we try same experiment with the ternary composite and we get good result and by this composite we get  $57 \text{ mmolh}^{-1}\text{g}^{-1}$  hydrogen.

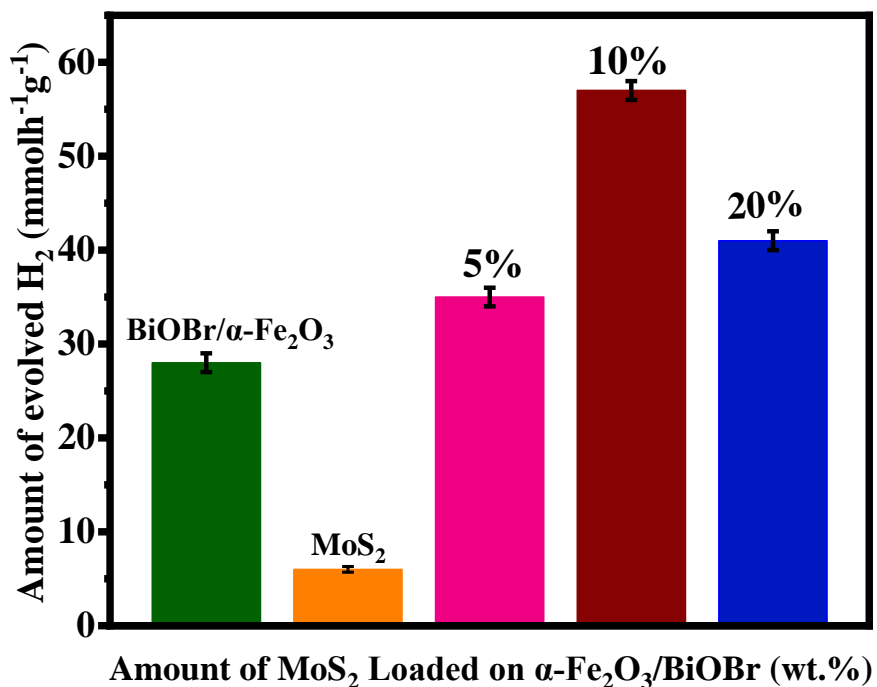


**Figure 27:** Comparison of Hydrogen production in Binary and Ternary Composites

Here is a bar graph showing hydrogen production by using ethanol as a sacrificial reagent.  $\text{MoS}_2$  has showing  $8 \text{ mmolh}^{-1}\text{g}^{-1}$   $\text{H}_2$  production. When it is loaded on binary composite  $\text{H}_2$  production increase instantly as we increase loading upto 10 %. After this it gradually start

decreasing. 10% of MoS<sub>2</sub> loading shows best results which is 57 mmolh<sup>-1</sup>g<sup>-1</sup>. And this is best production of this material.

### **5.3 Comparison of Hydrogen production in different morphologies of MoS<sub>2</sub>**

Here we also compare the hydrogen production rate with different morphologies of MoS<sub>2</sub>. First of all we synthesize multilayer nanosheets of MoS<sub>2</sub> and produced hydrogen from these multilayer. After this we try step by step with nanoparticles and with the few layer nanosheets of MoS<sub>2</sub>. As a results of all these reaction we get maximum results and maximum hydrogen production by few layer nanosheets of MoS<sub>2</sub>. Because these few layer provide more space for the reaction and suitable for the best production of the hydrogen. The reason behind this is few layer MoS<sub>2</sub> are completely etched and these layers are provide more space and surface area for the formation of the ternary composite. In this away few layer MoS<sub>2</sub> shows more hydrogen production than nanoparticle and multilayer sheets. These result we can easily see by this graph.

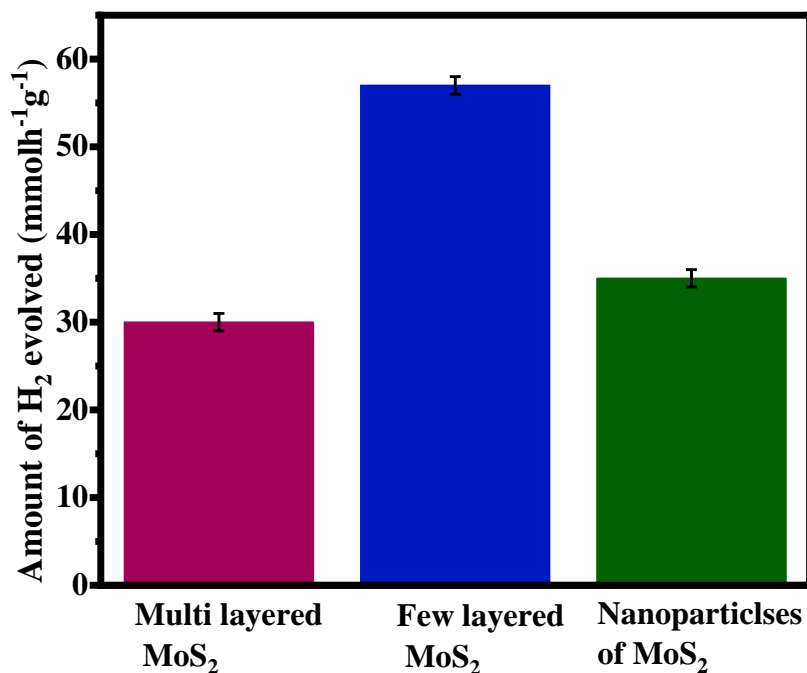


**Figure 28:** Comparison of Hydrogen production in different morphologies of MoS<sub>2</sub>

#### 5.4 Comparison with a different sacrificial agent

We also try it with different sacrificial reagents. Each sacrificial agent act as in different way and has different H<sub>2</sub> production value. Ethanol is a best sacrificial agent and have more hydrogen production than all others. Because it conserve all holes in the conduction band of the lower photocatalyst. All other sacrificial agent are good but less than ethanol. It is so commonly available and low cast sacrificial agent.

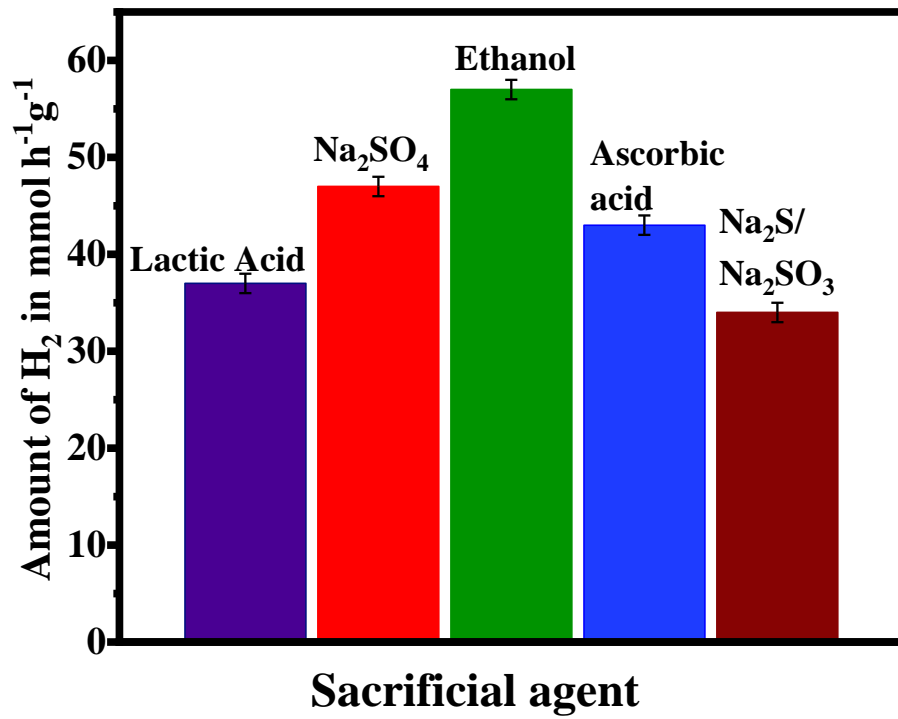


**Figure 29:** Comparison with a different sacrificial agent

## Chapter 6: Conclusion

This work investigated the first-ever synthesis of a novel S-Scheme 2D-2D  $\alpha$ -Fe<sub>2</sub>O<sub>3</sub>/BiOBr/MoS<sub>2</sub> heterojunction photocatalyst and its photocatalytic properties. Scientists discovered that the photocatalyst's stability might be improved by allowing photo-generated holes to quickly migrate out of  $\alpha$ -Fe<sub>2</sub>O<sub>3</sub> valence band. Reactive oxygen species (ROS) were verified to be produced as a result of the charge transfer synergy between BiOBr and  $\alpha$ -Fe<sub>2</sub>O<sub>3</sub>. SEM, TEM, HRTEM, PL, and Chronoamperometry were among the characterization methods utilized to support the catalyst's improved visible light harvesting and decreased charge recombination features. The flat band potential (V<sub>fb</sub>) measurement further supported the band potentials' aptitude for improved ROS generation. The catalyst showed excellent photocatalytic activity for the production of H<sub>2</sub> up to 57 mmolh<sup>-1</sup> g<sup>-1</sup>.

Because S-Scheme heterojunctions have not been investigated in the context of  $\alpha$ -Fe<sub>2</sub>O<sub>3</sub>/BiOBr photocatalysts, the findings of this study are significant. The study also demonstrates that the catalyst can be used for the production of hydrogen and to treat various contaminants and that more research can be done on the process of ROS formation. The catalyst might also be evaluated for applications involving the creation of hydrogen and the reduction of CO<sub>2</sub>. The study's main finding is that the synthetic 2D-2D  $\alpha$ -Fe<sub>2</sub>O<sub>3</sub>/BiOBr/MoS<sub>2</sub> heterojunction photocatalyst has the potential to be a reliable and effective photocatalyst for the production of hydrogen and the

removal of contaminants from wastewater. Future studies on the creation of effective photocatalysts for various environmental applications may find value in the study's findings.



## **Future Perspective**

### **Hydrogen Storage**

The most crucial component of a hydrogen economy is hydrogen capture and storage. Hydrogen storage materials made of a variety of materials are being researched. In order to make a hydrogen fuel system practical, hydrogen capturing, and Issues with storage and delivery must be thoroughly handled. In fact, it will be challenging to establish a hydrogen economy without effective and successful storage technologies [10, 88, 89].

### **Integration of hydrogen in electricity generation sector**

Currently, the globe produces electricity via traditional methods, in which chemical energy is transformed into thermal energy, mechanical energy, and eventually electricity. In contrast to the example given above, an intriguing device called a fuel cell may be able to turn chemical energy into electricity. Additionally, when our catalyst combines with water, hydrogen and a sizable amount of heat are produced, which might result in the production of hydrogen gas. The same steam and hydrogen can then be utilized in a turbine system to generate mechanical power (by burning, this will produce more heat [90, 91]).

## Chapter 7: References

- [1] H. Wei, C. Wang, S. Yang, B. Yin, Y. Huang, F. Yu, J. Han, Y. Lu, X. Liu, Integrated design of hydrogen production and thermal energy storage functions of Al-Bi-Cu composite powders, *International Journal of Hydrogen Energy*, 48 (2023) 14931-14940.
- [2] S.S. Mao, S. Shen, L. Guo, Nanomaterials for renewable hydrogen production, storage and utilization, *Progress in Natural Science: Materials International*, 22 (2012) 522-534.
- [3] M. Ball, M. Wietschel, The future of hydrogen – opportunities and challenges, *International Journal of Hydrogen Energy*, 34 (2009) 615-627.
- [4] S. Takenaka, Y. Shigeta, E. Tanabe, K. Otsuka, Methane decomposition into hydrogen and carbon nanofibers over supported Pd–Ni catalysts, *Journal of Catalysis*, 220 (2003) 468-477.
- [5] R.K. Ahluwalia, T.Q. Hua, J.K. Peng, On-board and Off-board performance of hydrogen storage options for light-duty vehicles, *International Journal of Hydrogen Energy*, 37 (2012) 2891-2910.
- [6] T. Hisatomi, K. Domen, Reaction systems for solar hydrogen production via water splitting with particulate semiconductor photocatalysts, *Nature Catalysis*, 2 (2019) 387-399.
- [7] L. Yu, J. Xi, CeO<sub>2</sub> nanoparticles improved Pt-based catalysts for direct alcohol fuel cells, *International Journal of Hydrogen Energy*, 37 (2012) 15938-15947.
- [8] S. McWhorter, C. Read, G. Ordaz, N. Stetson, Materials-based hydrogen storage: Attributes for near-term, early market PEM fuel cells, *Current Opinion in Solid State and Materials Science*, 15 (2011).
- [9] A. Züttel, P. Wenger, P. Sudan, P. Mauron, S.-i. Orimo, Hydrogen density in nanostructured carbon, metals and complex materials, *Materials Science and Engineering: B*, 108 (2004) 9-18.
- [10] A. Züttel, Hydrogen storage methods, *Naturwissenschaften*, 91 (2004) 157-172.
- [11] A. Machado, A. Patrocínio, M. França, L. Santos, K. Borges, L. Paula, Metal oxides for photoinduced hydrogen production and dye-sensitized solar cell applications, *Materials and processes for energy: communicating current research and technological developments*, 867 (2013).
- [12] A.E.H. Machado, L. Santos, K.A. Borges, P. Batista, V. Paiva, P.S. Müller Jr, D. Oliveira, M.D. França, Potential applications for solar photocatalysis: from environmental remediation to energy conversion, *Solar radiation*, 19 (2012) 339-378.
- [13] M. Varavipour, T. Asadi, M. Mashal, Application of two layers of soil with different textures for decreasing pollution from landfills to the subterranean water table, *RESEARCH ON CROPS*, 12 (2011) 833-838.
- [14] E.J. Weber, V.C. Stickney, Hydrolysis kinetics of reactive blue 19-vinyl sulfone, *Water Research*, 27 (1993) 63-67.
- [15] A. Anju, P. Ravi S, S. Bechan, Water pollution with special reference to pesticide contamination in India, *Journal of Water Resource and Protection*, 2010 (2010).
- [16] A. Haines, R.S. Kovats, D. Campbell-Lendrum, C. Corvalán, Climate change and human health: impacts, vulnerability and public health, *Public health*, 120 (2006) 585-596.
- [17] A.E. Machado, K.A. Borges, T.A. Silva, L.M. Santos, M.F. Borges, W.A. Machado, B.P. Caixeta, S.M. Oliveira, A.G. Trovó, A.O. Patrocínio, Applications of mesoporous ordered semiconductor materials—case study of TiO<sub>2</sub>, *Solar Radiation Applications*, (2015) 87-118.
- [18] A. Houas, H. Lachheb, M. Ksibi, E. Elaloui, C. Guillard, J.-M. Herrmann, Photocatalytic degradation pathway of methylene blue in water, *Applied Catalysis B: Environmental*, 31 (2001) 145-157.

- [19] A. Jaroenworarluck, N. Pijarn, N. Kosachan, R. Stevens, Nanocomposite TiO<sub>2</sub>-SiO<sub>2</sub> gel for UV absorption, *Chemical Engineering Journal*, 181 (2012) 45-55.
- [20] Y. Zhang, Y.-J. Heo, J.-W. Lee, J.-H. Lee, J. Bajgai, K.-J. Lee, S.-J. Park, Photocatalytic Hydrogen Evolution via Water Splitting: A Short Review, 8 (2018) 655.
- [21] T. Hirakawa, K. Sato, A. Komano, S. Kishi, C. Nishimoto, N. Mera, M. Kugishima, T. Sano, N. Negishi, H. Ichinose, Y. Seto, K. Takeuchi, Specific properties on TiO<sub>2</sub> photocatalysis to decompose isopropyl methylphosphonofluoridate and dimethyl methylphosphonate in Gas Phase, *Journal of Photochemistry and Photobiology A: Chemistry*, 264 (2013) 12-17.
- [22] J.-W. Chen, J.-W. Shi, X. Wang, H.-Y. Ai, H.-J. Cui, M.-I. Fu, Hybrid metal oxides quantum dots/TiO<sub>2</sub> block composites: Facile synthesis and photocatalysis application, *Powder Technology*, 246 (2013) 108-116.
- [23] J. Balbuena, Preparación de nuevos materiales fotocatalizadores para la descontaminación de gases NO<sub>x</sub>, 2017.
- [24] L. Hu, J. Wang, J. Zhang, Q. Zhang, Z. Liu, An N-doped anatase/rutile TiO<sub>2</sub> hybrid from low-temperature direct nitridization: enhanced photoactivity under UV-/visible-light, *RSC Advances*, 4 (2014) 420-427.
- [25] D.S. Kim, S.-Y.J.A.C.A.-g. Kwak, The hydrothermal synthesis of mesoporous TiO<sub>2</sub> with high crystallinity, thermal stability, large surface area, and enhanced photocatalytic activity, 323 (2007) 110-118.
- [26] D.S. Kim, S.J. Han, S.Y. Kwak, Synthesis and photocatalytic activity of mesoporous TiO<sub>2</sub> with the surface area, crystallite size, and pore size, *Journal of colloid and interface science*, 316 (2007) 85-91.
- [27] J.-L. Blin, M.-J. Stébé, T. Roques-Carmes, Use of ordered mesoporous titania with semi-crystalline framework as photocatalyst, *Colloids and Surfaces A: Physicochemical and Engineering Aspects*, 407 (2012) 177-185.
- [28] R.M. Cornell, U. Schwertmann, *The iron oxides: structure, properties, reactions, occurrences, and uses*, Wiley-vch Weinheim2003.
- [29] K. Sivula, F. Le Formal, M.J.C. Grätzel, Solar water splitting: progress using hematite ( $\alpha$ -Fe<sub>2</sub>O<sub>3</sub>) photoelectrodes, 4 (2011) 432-449.
- [30] J.H. Kennedy, K.W. Frese, Photooxidation of Water at  $\alpha$ -Fe<sub>2</sub>O<sub>3</sub> Electrodes, *Journal of The Electrochemical Society*, 125 (1978) 709.
- [31] G. Horowitz, Capacitance-voltage measurements and flat-band potential determination on Zr-doped  $\alpha$ -Fe<sub>2</sub>O<sub>3</sub> single-crystal electrodes, *Journal of Electroanalytical Chemistry and Interfacial Electrochemistry*, 159 (1983) 421-436.
- [32] C. Sanchez, K.D. Sieber, G.A. Somorjai, The photoelectrochemistry of niobium doped  $\alpha$ -Fe<sub>2</sub>O<sub>3</sub>, *Journal of Electroanalytical Chemistry and Interfacial Electrochemistry*, 252 (1988) 269-290.
- [33] K. Itoh, J.O.M. Bockris, Thin Film Photoelectrochemistry: Iron Oxide, *Journal of The Electrochemical Society*, 131 (1984) 1266.
- [34] T.K. Sinha, 14 - Morphology-dependent visible light photocatalysis, in: A.K. Nayak, N.K. Sahu (Eds.) *Nanostructured Materials for Visible Light Photocatalysis*, Elsevier2022, pp. 375-412.
- [35] G. Liao, C. Li, X. Li, B. Fang, Emerging polymeric carbon nitride Z-scheme systems for photocatalysis, *Cell Reports Physical Science*, 2 (2021) 100355.
- [36] J. Fu, Q. Xu, J. Low, C. Jiang, J. Yu, Ultrathin 2D/2D WO<sub>3</sub>/g-C<sub>3</sub>N<sub>4</sub> step-scheme H<sub>2</sub>-production photocatalyst, *Applied Catalysis B: Environmental*, 243 (2019) 556-565.

- [37] Q. Xu, L. Zhang, B. Cheng, J. Fan, J. Yu, S-Scheme Heterojunction Photocatalyst, *Chem*, 6 (2020) 1543-1559.
- [38] F. Mei, K. Dai, J. Zhang, W. Li, C. Liang, Construction of Ag SPR-promoted step-scheme porous g-C<sub>3</sub>N<sub>4</sub>/Ag<sub>3</sub>VO<sub>4</sub> heterojunction for improving photocatalytic activity, *Applied Surface Science*, 488 (2019) 151-160.
- [39] X. Jia, Q. Han, M. Zheng, H. Bi, One pot milling route to fabricate step-scheme Ag/I-BiOAc photocatalyst: Energy band structure optimized by the formation of solid solution, *Applied Surface Science*, 489 (2019) 409-419.
- [40] Q. Xu, L. Zhang, J. Yu, S. Wageh, A.A. Al-Ghamdi, M. Jaroniec, Direct Z-scheme photocatalysts: Principles, synthesis, and applications, *Materials Today*, 21 (2018) 1042-1063.
- [41] F. He, A. Meng, B. Cheng, W. Ho, J. Yu, Enhanced photocatalytic H<sub>2</sub>-production activity of WO<sub>3</sub>/TiO<sub>2</sub> step-scheme heterojunction by graphene modification, *Chinese Journal of Catalysis*, 41 (2020) 9-20.
- [42] J. Mu, F. Teng, H. Miao, Y. Wang, X. Hu, In-situ oxidation fabrication of 0D/2D SnO<sub>2</sub>/SnS<sub>2</sub> novel Step-scheme heterojunctions with enhanced photoelectrochemical activity for water splitting, *Applied Surface Science*, 501 (2020) 143974.
- [43] R. Wang, J. Shen, W. Zhang, Q. Liu, M. Zhang, Zulfiqar, H. Tang, Build-in electric field induced step-scheme TiO<sub>2</sub>/W<sub>18</sub>O<sub>49</sub> heterojunction for enhanced photocatalytic activity under visible-light irradiation, *Ceramics International*, 46 (2020) 23-30.
- [44] T. Hu, K. Dai, J. Zhang, G. Zhu, C. Liang, One-pot synthesis of step-scheme Bi<sub>2</sub>S<sub>3</sub>/porous g-C<sub>3</sub>N<sub>4</sub> heterostructure for enhanced photocatalytic performance, *Materials Letters*, 257 (2019) 126740.
- [45] D. Xu, Y. Rui, Y. Li, Q. Zhang, H.J.A.S.S. Wang, Zn-Co layered double hydroxide modified hematite photoanode for enhanced photoelectrochemical water splitting, 358 (2015) 436-442.
- [46] J. Li, F. Meng, S. Suri, W. Ding, F. Huang, N.J.C.c. Wu, Photoelectrochemical performance enhanced by a nickel oxide-hematite p-n junction photoanode, 48 (2012) 8213-8215.
- [47] X. Meng, Z.J.I.J.o.P. Zhang, Synthesis, analysis, and testing of BiOBr-Bi<sub>2</sub>WO<sub>6</sub> photocatalytic heterojunction semiconductors, 2015 (2015).
- [48] S. Shenawi-Khalil, V. Uvarov, S. Fronton, I. Popov, Y.J.T.J.o.P.C.C. Sasson, A novel heterojunction BiOBr/bismuth oxyhydrate photocatalyst with highly enhanced visible light photocatalytic properties, 116 (2012) 11004-11012.
- [49] X. Meng, Z.J.J.o.P. Zhang, P.A. Chemistry, Facile synthesis of BiOBr/Bi<sub>2</sub>WO<sub>6</sub> heterojunction semiconductors with high visible-light-driven photocatalytic activity, 310 (2015) 33-44.
- [50] H. Wang, D. Yong, S. Chen, S. Jiang, X. Zhang, W. Shao, Q. Zhang, W. Yan, B. Pan, Y. Xie, Oxygen-Vacancy-Mediated Exciton Dissociation in BiOBr for Boosting Charge-Carrier-Involved Molecular Oxygen Activation, *Journal of the American Chemical Society*, 140 (2018) 1760-1766.
- [51] G.S. Cao, G.L. Wang, Y.J. Bai, M.X.J.M. Liu, N. Letters, Photocatalytic removal of Rhodamine B using Fe<sub>3</sub>O<sub>4</sub>/BiOBr magnetic microsphere under visible-light irradiation, 10 (2015) 115-118.
- [52] C. Guo, Y. He, P. Du, X. Zhao, J. Lv, W. Meng, Y. Zhang, J.J.A.s.s. Xu, Novel magnetically recoverable BiOBr/iron oxides heterojunction with enhanced visible light-driven photocatalytic activity, 320 (2014) 383-390.
- [53] Y. Zhang, J. Ju, D. Wang, H. Yuan, L. Hao, Y. Tan, Aggregation-induced emission for the visualization of the structure and properties of polymers, *Journal of Materials Chemistry C*, 9 (2021) 11484-11496.

- [54] V. Luca, M. Osborne, D. Sizgek, C. Griffith, P.Z. Araujo, Photodegradation of Methylene Blue Using Crystalline Titanosilicate Quantum-Confined Semiconductor, *Chemistry of Materials*, 18 (2006) 6132-6138.
- [55] V.R. Posa, V. Annavaram, J.R. Koduru, P. Bobbala, M. V, A.R. Somala, Preparation of graphene-TiO<sub>2</sub> nanocomposite and photocatalytic degradation of Rhodamine-B under solar light irradiation, *Journal of Experimental Nanoscience*, 11 (2016) 722-736.
- [56] A. Fávaro Pipi, G. Soares, L. Ruotolo, Photocatalytic Activity and RNO Dye Degradation of Nitrogen-doped TiO<sub>2</sub> Prepared by Ionothermal Synthesis, *Materials Research*, 20 (2017).
- [57] H. Pouredal, A. Norozi, M. Keshavarz, A. Semnani, Nanoparticles of zinc sulfide doped with manganese, nickel and copper as nanophotocatalyst in the degradation of organic dyes, *Journal of hazardous materials*, 162 (2008) 674-681.
- [58] A. Wu, J. Li, B. Liu, W. Yang, Y. Jiang, L. Liu, X. Zhang, C. Xiong, X. Jiang, Band-gap tailoring and visible-light-driven photocatalytic performance of porous (GaN)<sub>1-x</sub>(ZnO)<sub>x</sub> solid solution, *Dalton Transactions*, 46 (2017) 2643-2652.
- [59] S.K. Dutta, S.K. Mehetor, N. Pradhan, Metal Semiconductor Heterostructures for Photocatalytic Conversion of Light Energy, *The journal of physical chemistry letters*, 6 (2015) 936-944.
- [60] T.B. Nguyen, R.-a. Doong, Fabrication of highly visible-light-responsive ZnFe<sub>2</sub>O<sub>4</sub>/TiO<sub>2</sub> heterostructures for the enhanced photocatalytic degradation of organic dyes, *RSC Advances*, 6 (2016) 103428-103437.
- [61] Y. Min, K. Zhang, Y. Chen, Y. Zhang, Synthesis of novel visible light responding vanadate/TiO<sub>2</sub> heterostructure photocatalysts for application of organic pollutants, *Chemical Engineering Journal - CHEM ENG J*, 175 (2011) 76-83.
- [62] N. Lubick, K. Betts, Silver socks have cloudy lining| Court bans widely used flame retardant, ACS Publications, 2008.
- [63] T. Feng, G.S. Feng, L. Yan, J.H.J.I.J.o.P. Pan, One-dimensional nanostructured TiO<sub>2</sub> for photocatalytic degradation of organic pollutants in wastewater, 2014 (2014).
- [64] V. Scuderi, G. Impellizzeri, L. Romano, M. Scuderi, G. Nicotra, K. Bergum, A. Irrera, B.G. Svensson, V.J.N.R.L. Privitera, TiO<sub>2</sub>-coated nanostructures for dye photo-degradation in water, 9 (2014) 1-7.
- [65] S.S. Bhat, N.G.J.N.J.o.C. Sundaram, Photocatalysis of Bi<sub>4</sub>NbO<sub>8</sub> hierarchical nanostructure for degradation of dye under solar/UV irradiation, 39 (2015) 3956-3963.
- [66] A. Fujishima, K. Honda, Electrochemical Photolysis of Water at a Semiconductor Electrode, *Nature*, 238 (1972) 37-38.
- [67] S. Yanagida, T. Azuma, Y. Midori, C. Pac, H.J.J.o.t.C.S. Sakurai, *Perkin Transactions 2, Semiconductor photocatalysis. Part 4. Hydrogen evolution and photoredox reactions of cyclic ethers catalysed by zinc sulphide*, (1985) 1487-1493.
- [68] M. Anpo, H. Yamashita, Y. Ichihashi, S. Ehara, Photocatalytic reduction of CO<sub>2</sub> with H<sub>2</sub>O on various titanium oxide catalysts, *Journal of Electroanalytical Chemistry*, 396 (1995) 21-26.
- [69] M.R. Hoffmann, S.T. Martin, W. Choi, D.W.J.C.r. Bahnemann, Environmental applications of semiconductor photocatalysis, 95 (1995) 69-96.
- [70] T. Kitamura, K. Maruo, Y. Wada, K. Murakoshi, T. Akano, S.J.J.o.t.C.S. Yanagida, *Chemical Communications, Photo-splitting of water to dihydrogen and hydroxyl radicals catalysed by rhodium-deposited perfluorinated poly (p-phenylene)*, (1995) 2189-2190.

- [71] R. Su, R. Bechstein, L. Sør, R.T. Vang, M. Sillassen, B.r. Esbjörnsson, A. Palmqvist, F.J.T.j.o.p.c.C. Besenbacher, How the anatase-to-rutile ratio influences the photoreactivity of TiO<sub>2</sub>, 115 (2011) 24287-24292.
- [72] Z. Wang, Q. Li, H. Xu, C. Dahl-Petersen, Q. Yang, D. Cheng, D. Cao, F. Besenbacher, J.V. Lauritsen, S. Helveg, M. Dong, Controllable etching of MoS<sub>2</sub> basal planes for enhanced hydrogen evolution through the formation of active edge sites, *Nano Energy*, 49 (2018) 634-643.
- [73] Z. Li, C. Kong, G.J.T.J.o.P.C.C. Lu, Visible photocatalytic water splitting and photocatalytic two-electron oxygen formation over Cu-and Fe-doped g-C<sub>3</sub>N<sub>4</sub>, 120 (2016) 56-63.
- [74] N. Xiao, S. Li, S. Liu, B. Xu, Y. Li, Y. Gao, L. Ge, G. Lu, Novel PtPd alloy nanoparticle-decorated g-C<sub>3</sub>N<sub>4</sub> nanosheets with enhanced photocatalytic activity for H<sub>2</sub> evolution under visible light irradiation, *Chinese Journal of Catalysis*, 40 (2019) 352-361.
- [75] M. Boudart, G. Djéga-Mariadassou, *Kinetics of heterogeneous catalytic reactions*, Princeton University Press 2014.
- [76] S. Iqbal, Spatial Charge Separation and Transfer in L-Cysteine Capped NiCoP/CdS Nano-Heterojunction Activated with Intimate Covalent Bonding for High-Quantum-Yield Photocatalytic Hydrogen Evolution, *Applied Catalysis B: Environmental*, 274 (2020) 119097.
- [77] Z. Pan, R. Wang, J. Li, S. Iqbal, W. Liu, K. Zhou, Fe<sub>2</sub>P nanoparticles as highly efficient freestanding co-catalyst for photocatalytic hydrogen evolution, *International Journal of Hydrogen Energy*, 43 (2018) 5337-5345.
- [78] S. Iqbal, Z. Pan, K. Zhou, Enhanced photocatalytic hydrogen evolution from in situ formation of few-layered MoS<sub>2</sub>/CdS nanosheet-based van der Waals heterostructures, *Nanoscale*, 9 (2017) 6638-6642.
- [79] H. Cheng, X.-J. Lv, S. Cao, Z.-Y. Zhao, Y. Chen, W.-F. Fu, Robustly photogenerating H<sub>2</sub> in water using FeP/CdS catalyst under solar irradiation, *Scientific Reports*, 6 (2016) 19846.
- [80] S. Cao, Y. Chen, C.-J. Wang, X.-J. Lv, W.-F. Fu, Spectacular photocatalytic hydrogen evolution using metal-phosphide/CdS hybrid catalysts under sunlight irradiation, *Chemical Communications*, 51 (2015) 8708-8711.
- [81] G. Chen, N. Ding, F. Li, Y. Fan, Y. Luo, D. Li, Q. Meng, Enhancement of photocatalytic H<sub>2</sub> evolution on ZnIn<sub>2</sub>S<sub>4</sub> loaded with in-situ photo-deposited MoS<sub>2</sub> under visible light irradiation, *Applied Catalysis B: Environmental*, 160-161 (2014) 614-620.
- [82] J.-X. Lv, Z.-M. Zhang, J. Wang, X.-L. Lu, W. Zhang, T.-B. Lu, In Situ Synthesis of CdS/Graphdiyne Heterojunction for Enhanced Photocatalytic Activity of Hydrogen Production, *ACS Applied Materials & Interfaces*, 11 (2019) 2655-2661.
- [83] Q. Xiang, F. Cheng, D. Lang, Hierarchical Layered WS<sub>2</sub>/Graphene-Modified CdS Nanorods for Efficient Photocatalytic Hydrogen Evolution, *ChemSusChem*, 9 (2016) 996-1002.
- [84] P. Wang, T. Wu, C. Wang, J. Hou, J. Qian, Y. Ao, Combining Heterojunction Engineering with Surface Cocatalyst Modification To Synergistically Enhance the Photocatalytic Hydrogen Evolution Performance of Cadmium Sulfide Nanorods, *ACS Sustainable Chemistry & Engineering*, 5 (2017) 7670-7677.
- [85] J. Zhang, L. Li, Z. Xiao, D. Liu, S. Wang, J. Zhang, Y. Hao, W. Zhang, Hollow Sphere TiO<sub>2</sub>-ZrO<sub>2</sub> Prepared by Self-Assembly with Polystyrene Colloidal Template for Both Photocatalytic Degradation and H<sub>2</sub> Evolution from Water Splitting, *ACS Sustainable Chemistry & Engineering*, 4 (2016) 2037-2046.
- [86] Y. Jin, L. Dang, H. Zhang, C. Song, Q. Lu, F. Gao, Synthesis of unit-cell-thick  $\alpha$ -Fe<sub>2</sub>O<sub>3</sub> nanosheets and their transformation to  $\gamma$ -Fe<sub>2</sub>O<sub>3</sub> nanosheets with enhanced LIB performances, *Chemical Engineering Journal*, 326 (2017) 292-297.

- [87] T. Simon, N. Bouchonville, M.J. Berr, A. Vaneski, A. Adrović, D. Volbers, R. Wyrwich, M. Döblinger, A.S. Susha, A.L. Rogach, F. Jäckel, J.K. Stolarczyk, J. Feldmann, Redox shuttle mechanism enhances photocatalytic H<sub>2</sub> generation on Ni-decorated CdS nanorods, *Nature Materials*, 13 (2014) 1013-1018.
- [88] M. Balat, Potential importance of hydrogen as a future solution to environmental and transportation problems, *International Journal of Hydrogen Energy*, 33 (2008) 4013-4029.
- [89] G.W. Crabtree, M.S. Dresselhaus, *The Hydrogen Fuel Alternative*, *MRS Bulletin*, 33 (2008) 421-428.
- [90] F. Franzoni, M. Milani, L. Montorsi, V. Golovitchev, Combined hydrogen production and power generation from aluminum combustion with water: Analysis of the concept, *International Journal of Hydrogen Energy*, 35 (2010) 1548-1559.
- [91] S. Mercati, M. Milani, L. Montorsi, F. Paltrinieri, Optimization of the working cycle for a hydrogen production and power generation plant based on aluminum combustion with water, *International Journal of Hydrogen Energy*, 38 (2013) 7209–7217.